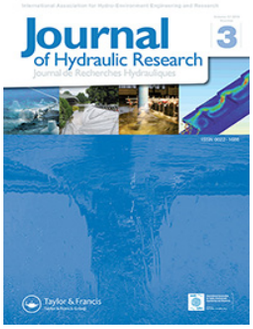

Journal of Hydraulic Research

ISSN: 0022-1686 (Print) 1814-2079 (Online) Journal homepage: https://www.tandfonline.com/loi/tjhr20

Formulation of consistent finite volume schemes for hydraulic transients

Sara Mesgari Sohani & Mohamed Salah Ghidaoui

To cite this article: Sara Mesgari Sohani & Mohamed Salah Ghidaoui (2019) Formulation of consistent finite volume schemes for hydraulic transients, Journal of Hydraulic Research, 57:3, 353-373, DOI: 10.1080/00221686.2018.1522377

To link to this article: https://doi.org/10.1080/00221686.2018.1522377

Published online: 20 Dec 2018.

Journal of Hydraulic Research Vol. 57, No. 3 (2019), pp. 353–373
https://doi.org/10.1080/00221686.2018.1522377

Research paper

Formulation of consistent finite volume schemes for hydraulic transients

SARA MESGARI SOHANI, Graduate MPhil Student, *Civil Department, Hong Kong University of Science and Technology, Hong Kong, PR China*
Email: cemesgari@connect.ust.hk (author for correspondence)

MOHAMED SALAH GHIDAOUI (IAHR Member), Chinese Estates Professor of Engineering and Chair Professor *Civil Department, Hong Kong University of Science and Technology, Hong Kong, PR China*
Email: ghidaoui@ust.hk

ABSTRACT
Intentionally generated transient waves are used in the detection of defects in pipelines. Experience to date in these applications shows that the wider the band of injected wave frequencies the better is the detection effectiveness. Thus, as these technologies develop further, models that can handle high frequency waves will be required. Finite volume (FV) methods are well suited for high frequency wave phenomena, but their use in the water hammer field has been limited to date compared with other fields such as open channel flow. A major reason for this is that FV methods are formulated for simple boundary conditions such as no-flux or no-slip, but have not been well developed for the typically more complex boundary conditions found in pressurized pipeline systems (e.g. junctions, control valves, orifices, tanks and reservoirs). In those few instances in the literature where FV has been applied to water hammer problems, the approach has been to use FV for internal sections and method of characteristics (MOC) at the boundaries. The global order of accuracy of FV–MOC is governed by the MOC solution. To our knowledge, this paper constitutes a first attempt at handling boundary conditions within the FV framework. The approach places the boundary element within a FV to enforce mass and momentum conservation within this volume. The fluxes between the FV and the adjacent elements are then formulated in the usual manner. The approach is illustrated for the case of a valve, a reservoir and a junction. The finite volume method used is the Boltzmann-type scheme. The accuracy and efficiency of all schemes with the proposed non-iterative FV formulation of the boundary conditions are demonstrated through the following test cases: (i) water hammer wave interactions with a junction boundary characterized by a geometric discontinuity, (ii) water hammer wave interactions with a junction boundary characterized by a discontinuity in the value of wave speed, and (iii) water hammer wave interactions with a junction characterized by a flow rate discontinuity. The pure FV formulation guarantees mass and momentum conservation. The Boltzmann-based FV schemes capture discontinuity as well as wave interactions with boundary elements accurately. The stability of the proposed FV schemes is satisfied when $C_r < 0.5$.

Keywords: Boltzmann method; boundary condition; finite volume; high frequency wave; water hammer

1 Introduction

Pressurized pipeline systems are key infrastructure in the water, oil, and gas industries. These systems transport fluids from source to treatment and from treatment to point(s) of consumption. In addition to the pipe components themselves, these systems include a large number of devices (e.g. valves, pumps and tanks) whose role is to move, store or control flow and pressure and to maintain them at desired levels. These devices are distinguishable from the pipes by their small length scale in comparison to the length scale of pipes. As a result, the traditional approach to solving the flow equation in a pipe is to treat the devices as localized boundary conditions (Chaudhry, 1979; Karney, 1984).

Sudden flow disturbances caused either accidentally or deliberately by these devices or boundary conditions can trigger fast, large, and even destructive waves that propagate throughout the pipe system and continually interact with devices. From the structural integrity point of view, engineers need to estimate how large the potential amplitude of critical generated pressure waves is in both the negative (pressure decrease) and positive (pressure increase) sense. Extreme positive pressure waves can cause catastrophic system failure , e.g. the Russian hydroelectric plant disaster (Hasler, 2010). Extreme negative pressure waves can lead to cavitation-induced failures (Siemons, 1967) and may increase the cross-contamination risk through nearby cracks or pipeline joints (Ebacher, Besner, Prévost, & Allard, 2010; LeChevallier, Gullick, Karim, Friedman, & Funk, 2003).

Received 31 July 2016; accepted 7 September 2018/Open for discussion until 31 December 2019.

ISSN 0022-1686 print/ISSN 1814-2079 online
http://www.tandfonline.com

Moreover, the occurrence of transient waves in water supply systems may also adversely affect the quality of drinking water since sudden flow changes also may cause sediment and biofilm detachment, leading to discoloration and loss of residual chlorine (Aisopou, Stoianov, & Graham, 2010). Other possible impacts of transient waves include excessive noise, fatigue, pitting due to cavitation, disruption of normal control, and a destructive resonant vibration associated with the inherent period of certain pipe systems.

Not all transient pressure waves are bad. Research conducted in the past 20 years shows that planned and controlled transient waves are beneficially used in the detection of defects such as leakage and blockage in pipelines without disruptive access to the pipe network. Defects such as leakages, which are a major and widespread problem in pressurized pipe systems, contribute roughly 30% to water loss in water supply systems (Thornton, Sturm, & Kunkel, 2008). The detection attributes of transient waves are: (i) rapidity, since they propagate at speeds of 400–1000 m s^{-1}; (ii) efficiency, since they contain a wealth of information on all parts of the system through which they propagate; and (iii) non-destructiveness, since they do not require system alteration. The signature of different defects on transient waves can be rapidly collected using a finite number of locations (e.g. access-points to pipe networks) and can be used to extract and identify defect parameters in a post-processing step (Brunone, 1999; Duan, Lee, Ghidaoui, & Tung, 2012; Liou, 1998; Mohapatra, Chaudhry, Kassem, & Moloo, 2006; Stephens, Lambert, Simpson, Vítkovskỳ, & Nixon, 2004).

While research in the past 20 years has showed significant potential of transient-based detection methods, only recently has the importance of high frequency waves and model accuracy to defect detection been pointed out (Duan et al., 2012; Stephens et al., 2004). Therefore, it would seem imperative that the numerical models used have a higher order of accuracy. Among the many numerical methods applied to transients (e.g. method of characteristics (MOC), wave plan (WP), finite difference (FD), finite element (FE), finite volume (FV), and corrective smoothed particle method (CSPM)), FV methods are known to be well suited for high frequency waves (Luo & Xu, 2013; Luo, Xuan, & Xu, 2013). However, FV methods have traditionally been formulated only for simple boundary conditions such as the Neumann, Dirichlet or Robin conditions. FV methods have not been formulated for the more complex and ubiquitous types of boundary conditions that are present in pipe systems such as valves, junctions and pumps. Such boundary conditions are generally in the form of pressure-flow relations that are nonlinear, implicit, time-dependent and not rendered easily amenable to the FV framework.

Conventionally, these boundary conditions are straightforwardly handled in the MOC framework by defining the mathematical expressions to relate pressure head and discharge. MOC was first applied to water hammer by Streeter and Lai (1962). Streeter and Wylie (1967) extended MOC to handle boundary conditions for a few simple systems. Chaudhry (1968, 1979) developed boundary conditions for reservoirs, sprinklers, valves, surge tanks and air chambers. Karney (1984) developed an algorithm to perform comprehensive transient analysis of networks with arbitrary complexity in which he presents concise terminology for describing pipe networks and boundary conditions. McInnis (1993) formulated a unified set of boundary conditions that handles devices and layouts that are found in practical water supply systems. Axworthy (1997) developed boundary conditions that are consistent with quasi-steady state, rigid water column, and water hammer theories. These developments led to comprehensive treatment of various boundary conditions such as valves, pumps, turbines, accumulators, air valves and many others and helped cement the key role of MOC in engineering practice. In fact, Ghidaoui, Zhao, McInnis, and Axworthy (2005) reported that 11 out of 14 commercially available water hammer software packages are based on MOC. Comprehensive treatment of various boundary conditions can be found in research papers written by Streeter and Wylie (1967), Wylie, Streeter, and Suo (1993), Karney (1984), Chaudhry (1968), Chaudhry and Hussaini (1985), McInnis (1993), Axworthy (1997). However, in spite of all the advantages of MOC, MOC is problematic where the wave speed variation is large, due to presence of air or wall thinning. MOC, also, cannot be easily extended to two-dimensional and three-dimensional models because the characteristic relationships are not lines but become surfaces of cones and surfaces of spheres, respectively.

The treatment of boundary conditions in FV methodology is not straightforward. Guinot (1998) used a high-order, monotonic numerical scheme of the Godunov method to simulate water hammer waves in a FV framework. He proposed nine options to handle boundary conditions in a reservoir-pipe-valve system, and only one combination among the nine is shown to provide good results. Conventionally, a junction boundary is treated using either an iterative or non-iterative method to guarantee a single value of pressure and momentum at the junction (Chae, Lee, Hwang, & Lee, 2006; Kriel, 2012). Guinot (1998) also suggested an iterative treatment for the junction boundary conditions. Often, where FV has been applied to water hammer problems, the approach has been to use FV for internal sections and MOC at the boundaries (Zhao & Ghidaoui, 2004). Such FV–MOC hybridization means that the global order of accuracy is governed by the scheme with the lowest order of accuracy, which is invariably the MOC solution. The order of accuracy of the MOC solution degrades due to discretization problems that rise when modeling multi-pipe systems.

A non-iterative FV method for junction boundary treatment was developed by Hong and Kim (2011). A ghost junction cell was implemented while considering linear momentum interchange and wall effects. In their proposed model the RoeM scheme (i.e. the modified Roe scheme Kim, Kim, Rho, & Hong, 2003) is used to conserve mass and momentum and, at the same time, the stagnation enthalpy across the geometric discontinuity is preserved. In particular, their attempt to simulate

wave–system interactions at a junction characterized by a geometry discontinuity was flawed. Their numerical results differ from the analytical solutions and involve significant overshoots and undershoots. The origin of this discrepancy is likely due to the way they enforce enthalpy conservation.

The major driving force behind the current study is the need for a pure FV numerical model suitable for (i) high frequency waves and (ii) high wave speed variation. Note that not all FV schemes are suitable for high frequency waves. For instance, Louati (2013) pointed that a two-dimensional Riemann-based finite volume scheme numerically dissipates high frequency waves for transient flow in pipes. The mesoscopic-based schemes used in the current study can be easily extended to a non-dissipative model of order three or higher (Luo & Xu, 2013; Luo et al., 2013).

In the next section, the numerical implementations of boundary conditions are developed within a Boltzmann-based finite volume approach.

2 Governing equations

In the finite volume approach, the integral formulation of the mass and momentum conservation laws is applied on a physical space as follows (Hirsch, 2007):

$$\frac{\partial}{\partial t}\int_{\mathrm{CV}}\begin{bmatrix}\rho\\ \rho u\end{bmatrix}\mathrm{d}\mathcal{V}+\oint_{\mathrm{CS}}\begin{bmatrix}\rho u\\ \rho u^2+P\end{bmatrix}\cdot\vec{s}\,\mathrm{d}A=\boldsymbol{q} \tag{1}$$

where CV denotes control volume; CS denotes control surface; ρ is the density; A is the area; $\mathcal{V}$ is the volume; u is the flow velocity in x-direction which is equal to the average flow velocity in x-direction (i.e. U) in the current one-dimensional water hammer model; $\vec{s}$ is the outward normal unit vector (perpendicular to surface area); $\boldsymbol{q}$ is designated sink/source terms, and P is the pressure. For gas flow problems, P is coupled with flow density and temperature through the gas flow state equation. In water hammer, however, temperature is decoupled from pressure due to relatively large specific heat of water. Thus, the state equation fitted for water hammer applications is $\mathrm{d}P/\mathrm{d}\rho = a^2$, where a is transient wave speed (Chaudhry, 1979). The time-dependent mass and momentum fluxes on the control surface can be obtained after integrating Eq. (1) with respect to t. The time-dependent mass and momentum fluxes denoted $\overset{\mathrm{Mass}}{F}$ and $\overset{\mathrm{Mom}}{F}$, respectively are:

$$\begin{bmatrix}\overset{\mathrm{Mass}}{F}\\ \overset{\mathrm{Mom}}{F}\end{bmatrix}=\int\begin{bmatrix}\rho u\\ \rho u^2+P\end{bmatrix}\mathrm{d}t \tag{2}$$

Mesgari Sohani and Ghidaoui (2018) successfully formulated the second-order Bhatnagar–Gross–Krook (BGK) and the kinetic flux vector splitting (KFVS) schemes for a classical reservoir-pipe-valve water hammer test case in a finite volume framework. They calculated time-dependent fluxes on surface volumes using Boltzmann-based equations. In order to compare the classical water hammer solution to the proposed unified finite volume scheme, a map suggested by Mesgari Sohani and Ghidaoui (2018) to relate ρ and ρu to H and Q is represented below:

$$H=\frac{\rho a^2}{9.81\rho_0},\quad Q=\frac{\rho UA}{\rho_0} \tag{3}$$

where ρ_0 is the density before any disturbance, and A is the pipe cross-sectional area. Using the map, the numerical results associated with the KFVS and BGK schemes can be represented in the form of pressure head, notwithstanding that the original governing equations solve density and mass flux. In the current paper all fluxes (i.e. at pipes and boundaries) are calculated using the BGK and KFVS schemes to solve transient waves inside pipes.

It is worth mentioning that in the classical water hammer model, wave speed includes both water and pipe wall effects in the formulation (Chaudhry, 1979), whereas in the mesoscopic-based approaches, wave speed only bears the elasticity of fluid and excludes the wall effects (i.e. the rigid pipe assumption). In other words, the mesoscopic-based models solve fluid in pipes and exclude any interaction between fluid and pipe wall. To include the wall elasticity in the current formulation, however, the mesoscopic-based models are able to adopt the wall elasticity effect as external forces in formulation. Such a practice is out of the scope of the current study and is left for future studies.

3 Numerical schemes

In the one-dimensional water hammer framework, Eq. (1) is traditionally applied to the flow inside a pipe (Zhao & Ghidaoui, 2004) and auxiliary relations are used at the devices. In this paper, Eq. (1) is enforced everywhere in the pipe system, where a device is contained within a control volume (CV). The fluxes between the CV that contains the boundary element and the adjacent cells are then formulated using a FV method. In the current paper the finite volume methods used are the BGK and KFVS methods (i.e. mesoscopic-based methods) formulated by Mesgari Sohani and Ghidaoui (2018) for a classical water hammer test case and are extended to moderately complex pipe network systems.

Figure 1a sketches a pipe network including the boundary elements (e.g. valve, junction, reservoir and pump) and defects (e.g. leak, blockage and thinning wall). In Fig. 1b, all boundary elements are replaced with CVs indicated by the red colour, and defects (i.e. a sort of boundary condition) are replaced with purple-coloured CVs. The CV is able to take different geometries into account but is a lumped representation of a boundary condition and does not provide the flow details within it.

The one-dimensional representation of the unified FV method is illustrated in Fig. 2a for a simple pipe network with no

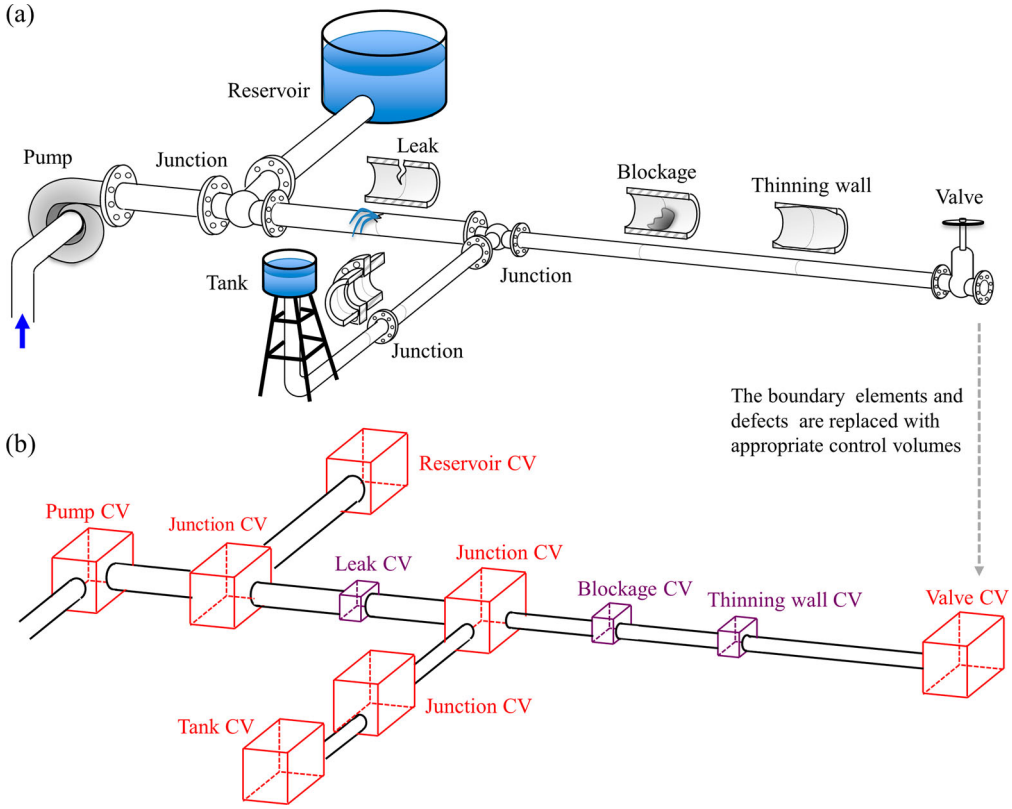

Figure 1 (a) Pipe network with boundary elements and defects. (b) The conceptual model to handle boundary conditions

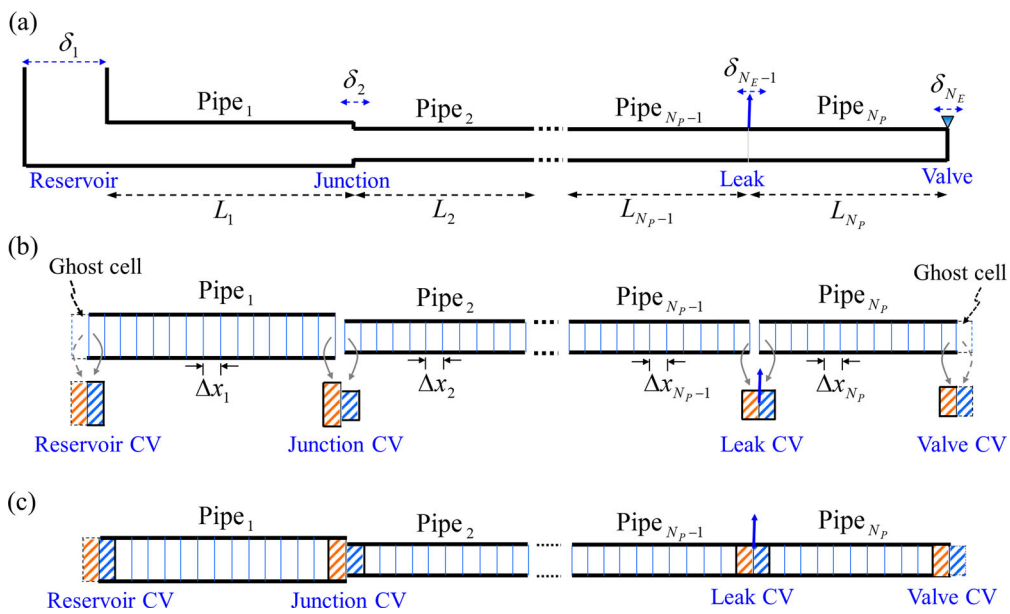

Figure 2 (a) Schematic of a pipe network with boundary elements. (b) Discrete space domain in pipes and control volumes associated with control elements. (c) The unified FV approached in a discrete space

friction but with boundary elements such as a junction, a valve and a reservoir. The number of pipes and elements are denoted by N_P and N_E, respectively. The length of elements, generally, is quite small in comparison with the length scale of pipes (i.e. $\delta_{k'}/L_k \ll 1$, where $k \in [1, N_P]$; $k' \in [1, N_E]$; L_k is the length of pipe k; and $\delta_{k'}$ is the length of element k').

Figure 2b shows a discrete space domain in which all pipes are uniformly discretized, so $\Delta x_k = L_k/N_k$, where $k \in [1, N_P]$; N_k is the number of cells in pipe k; and Δx_k is the cell size in pipe k. For such a multi-pipe system, the number of numerical cells in the entire computational domain is the sum of N_k where $k \in [1, N_P]$ and is denoted by N_x. Geometrically flexible CVs shown

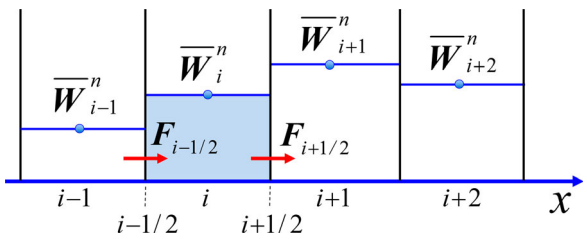

Figure 3 Discrete space domain

in Fig. 2b are utilized for boundary elements. Each CV includes two sub-cells. The left and right sub-cells are denoted by orange and blue colours, respectively. The interface between two sub-cells is called the boundary interface, where all the physics of a boundary element with the length scale of δ are numerically located.

The flexible CVs are placed either between two pipes (e.g. a junction CV and a leak CV) or at the end of a pipe (e.g. a reservoir CV and a valve CV) as shown in Fig. 2b. Where a boundary element is connected to two pipes, the left and right sub-cells of the CV lie in the end cells of pipes connected to a boundary element. While an element is attached to a pipe, one of the sub-cells, either the left one or the right one, is placed with a ghost cell (i.e. an imaginary cell outside of the pipe domain).

Figure 2c shows a one-dimensional representation of the unified FV method after placing CVs associated with the boundary elements. In the following sections the unified FV method is developed separately, first for an intact pipe and then for a few boundary elements.

3.1 *Discrete FV governing equations for an intact pipe*

Figure 3 shows a one-dimensional discrete space domain (i.e. a pipe of length L), which is equally discretized to N cells of width Δx (i.e. $\Delta x = L/N$). Cell (i), $i \in [1, N]$, is confined to the interface $x = x_{i-1/2}$ and the interface $x = x_{i+1/2}$. The flow variables are assumed to be the piecewise constant, namely $\overline{\boldsymbol{W}}_i^n = [\overline{\rho}_i^n, \overline{\rho u}_i^n]^{\mathrm{T}}$ inside cell (i) at time step n. The over-line notation indicates the cell-averaged flow variables. $\boldsymbol{F}_{i-1/2}$ and $\boldsymbol{F}_{i+1/2}$ are numerical fluxes across the interface $x = x_{i-1/2}$ and the interface $x = x_{i+1/2}$, respectively.

For a finite volume scheme (i.e. a CV of width Δx), the cell-average conservative variables $\overline{\boldsymbol{W}}_i$ inside cell i evolve from time t^n to t^{n+1} as follows:

$$\overline{\boldsymbol{W}}_i^{n+1} = \overline{\boldsymbol{W}}_i^n + \frac{1}{\Delta x}(\boldsymbol{F}_{i-1/2} - \boldsymbol{F}_{i+1/2}) \tag{4}$$

where

$$\Delta x = x_{i+1/2} - x_{i-1/2}, \quad \overline{\boldsymbol{W}} = \begin{bmatrix} \overline{\rho} \\ \overline{\rho u} \end{bmatrix}, \quad \boldsymbol{F} = \begin{bmatrix} \text{Mass} \\ F \\ \text{Mom} \\ F \end{bmatrix} \tag{5}$$

where $\boldsymbol{F}_{i-1/2}$ and $\boldsymbol{F}_{i+1/2}$ are the time-dependent fluxes at the interface $x = x_{i-1/2}$ and the interface $x = x_{i+1/2}$, respectively (i.e. flux-in and flux-out).

3.2 *Discrete FV governing equations specified for boundary elements*

The proposed FV approach is illustrated in this paper for a junction, a sudden valve closure, a fully open valve, and a reservoir boundary conditions.

Junction boundary condition characterized by a geometric discontinuity

In pipeline systems, changes in the size of pipe area are inevitable for two main reasons: (i) design criteria and (ii) blockages. Referring to the design criteria, the diameter of a pipe is intentionally altered in order to keep the flow variables within specified ranges and to minimize overall cost. In the case of a blockage, however, the original design cross-sectional area of a pipe is diminished because of wall deposition. These two features can be classified as junction boundary conditions on the basis of the geometric discontinuity they present to the flow.

Figure 4 shows a spatial grid for a multi-pipe system. In the computational domain, cell $(i = N)$ in pipe 1 is attached to cell $(j = 1)$ in pipe 2 where i and j are cell indices associated with pipe 1 and pipe 2, respectively. The cross-sectional area changes abruptly across the junction. The cross-sectional areas of pipe 1 and pipe 2 are denoted by A_1 and A_2, respectively. The wave speed magnitude is held constant over the entire computational domain. A junction CV including two sub-cells is specified such that the left sub-cell lies in cell $(i = N)$ and the right sub-cell lies in cell $(j = 1)$ and the effect of the vertical wall is replaced by external forces (i.e. F'_{Junction}). The boundary interface, and the

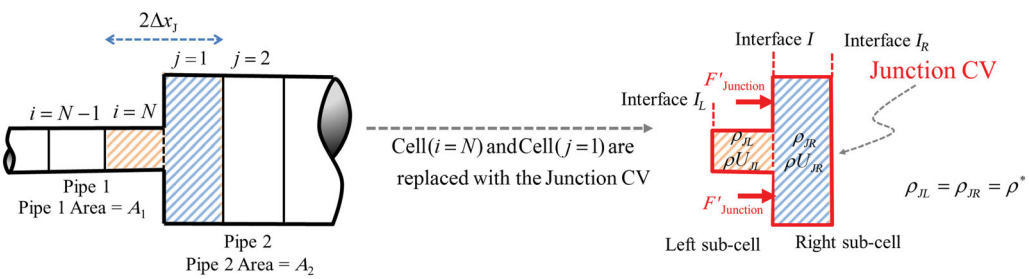

Figure 4 The discrete computational domain and the junction boundary condition characterized by a geometric discontinuity

left and right interfaces of the junction CV are denoted by the interface I, the interface I_L and the interface I_R, respectively. The flow variables inside the left and right sub-cells, respectively adopted from those inside cell ($i = N$) and cell ($j = 1$), are distinguished by subscripts $_{JL}$ and $_{JR}$ (Fig. 4). The size of the junction CV is denoted by $2\Delta x_J$, assuming the size of the sub-cells is identical and $\Delta x_J = \Delta x$. Although the tests are conducted for cases where the spatial reaches in either side of a boundary are the same, this is not a requirement and the schemes can be applied to different size of reaches on either side of a boundary.

A junction characterized by a geometry discontinuity is physically required to (i) maintain constant pressure across the junction (Benson, Woollatt, & Woods, 1963; Corberan, 1992; Wylie et al., 1993) and (ii) conserve mass and momentum across the junction. The geometric discontinuity, however, violates the conservation condition because the neighbouring cells at the junction (i.e. cell ($i = N$) and cell ($j = 1$)) do not have a common side (Hirsch, 2007). To deal with the problem, the integral forms of the mass conservation laws from time t^n to t^{n+1} are applied on the junction CV as follows (Streeter, Wylie, & Bedford, 1998):

$$\frac{1}{\Delta t}\left(\left[\int_{\forall}\rho\,\mathrm{d}\forall\right]^{n+1}-\left[\int_{\forall}\rho\,\mathrm{d}\forall\right]^{n}\right)+\int_{I_L}\rho U\,\mathrm{d}A-\int_{I_R}\rho U\,\mathrm{d}A=0 \tag{6}$$

where $\forall$ is the volume of the junction cell; U is the average velocity in x-direction; ρ is the density; A is the pipe cross-sectional area; n is time step; and $\Delta t = t^{n+1} - t^n$. The common pressure condition (i.e. $P_{JL} = P_{JR}$) in the junction implies the common fluid density, denoted by ρ^*, in the sub-cells. Therefore, Eq. (6) can be simplified as follows:

$$\frac{\Delta x_J}{\Delta t}(A_1+A_2)\left([\rho^*]^{n+1}-[\rho^*]^{n}\right)+\int_{I_L}\rho U\,\mathrm{d}A-\int_{I_R}\rho U\,\mathrm{d}A=0 \tag{7}$$

The fluid density inside the sub-cells can be evolved from time t^n to time t^{n+1} as follows:

$$[\rho^*]^{n+1}=[\rho^*]^{n}+\frac{\Delta t}{\Delta x_J}\frac{1}{(A_1+A_2)}\left(A_1\overset{\text{Mass}}{F_{I_L}}-A_2\overset{\text{Mass}}{F_{I_R}}\right) \tag{8}$$

where $\overset{\text{Mass}}{F_{I_L}}$ is the time-dependent mass flux-in at the interface I_L; and $\overset{\text{Mass}}{F_{I_R}}$ is the time-dependent mass flux-out at the interface I_R. Similarly, the momentum conservation law is applied to the junction CV and gives:

$$\left([\rho^*U_{JL}A_1+\rho^*U_{JR}A_2]^{n+1}-[\rho^*U_{JL}A_1+\rho^*U_{JR}A_2]^{n}\right)\frac{\Delta x_J}{\Delta t}=A_1\overset{\text{Mom}}{F_{I_L}}-A_2\overset{\text{Mom}}{F_{I_R}}+F'_{Junction} \tag{9}$$

where $F'_{Junction}$ is the force exerted in x-direction on the junction wall shown in Fig. 4. Since the mass flow rates, denoted by $\dot{m}^*$, inside the sub-cells are constant (i.e. $\dot{m}^* = \rho^* U_{JL}A_1 = \rho^* U_{JR}A_2$), Eq. (9) can be simplified as follows:

$$[\dot{m}^*]^{n+1}=[\dot{m}^*]^{n}+\frac{\Delta t}{2\Delta x_J}\left(A_1\overset{\text{Mom}}{F_{I_L}}-A_2\overset{\text{Mom}}{F_{I_R}}+F'_{Junction}\right) \tag{10}$$

$F'_{Junction}$ is a function of the fluid density adjacent to the wall (i.e. ρ^*) and is represented below:

$$F'_{Junction}=(A_2-A_1)a^2\frac{1}{2}\left([\rho^*]^{n}+[\rho^*]^{n+1}\right) \tag{11}$$

The form of Eq. (11) takes into account not only the flow information at time t^{n+1} but also the history of the flow at time t^n, i.e. an implicit form (Hirsch, 2007). From Eqs (8) and (10), ρ^* and $\dot{m}^*$ can be calculated at time step $n+1$. Then, U_{JL} and U_{JR} at time step $n+1$ can be calculated from ρ^* and $\dot{m}^*$ at time step $n+1$.

Junction boundary condition characterized by a discontinuity in the value of wave speed

In practice, when two pipes meet at a junction, their characteristics such as material or thickness may be different. The result is that the wave speed can vary from one pipe to another. Such variations are important in defect detection methods that rely on frequency shifts.

Figure 5 shows a computational domain including two pipes, which is uniformly discretized. In the computational domain, cell ($i = N$) in pipe 1 is attached to cell ($j = 1$) in pipe 2 where i and j are cell indices associated with pipe 1 and pipe 2, respectively. The cross-sectional areas of pipe 1 and pipe 2 are denoted by A_1 and A_2, respectively. The cross-sectional areas of pipes is held constant over the entire computational domain, so $A_1 = A_2 = A$. The material of pipe 1 is different from that of pipe 2. This means that a water hammer wave travels with different speed inside two pipes.

To treat the junction boundary condition characterized by a discontinuity in the value of wave speed, a junction CV including two sub-cells is used such that the left sub-cell lies in cell ($i = N$) and the right sub-cell lies in cell ($j = 1$). The boundary interface, and left and right interfaces of the junction CV are denoted by interface I, interface I_L and interface I_R, respectively. The flow variables inside the sub-cells, taken from those inside cell ($i = N$) and cell ($j = 1$), are distinguished by subscripts $_{JL}$ and $_{JR}$ for the left sub-cell and the right sub-cell, respectively (Fig. 5). The size of the junction CV is denoted by $2\Delta x_J$ assuming the size of the sub-cells is the same. In the current study, $\Delta x_J = \Delta x$.

Similar to the formulation in the previous section, the integral form of the mass and momentum equations for the junction CV, shown in Fig. 5, can be obtained. One major difference in the formulation is that a common pressure at the junction of two pipes does not imply a common flow density because

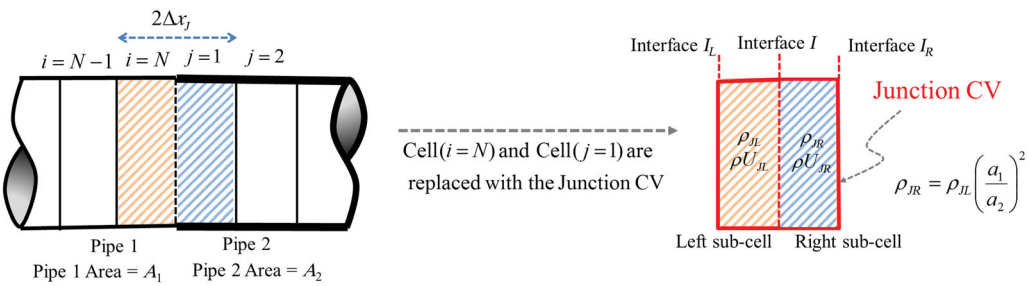

Figure 5 The discrete computation domain and the junction boundary condition characterized by a discontinuity in the value of wave speed

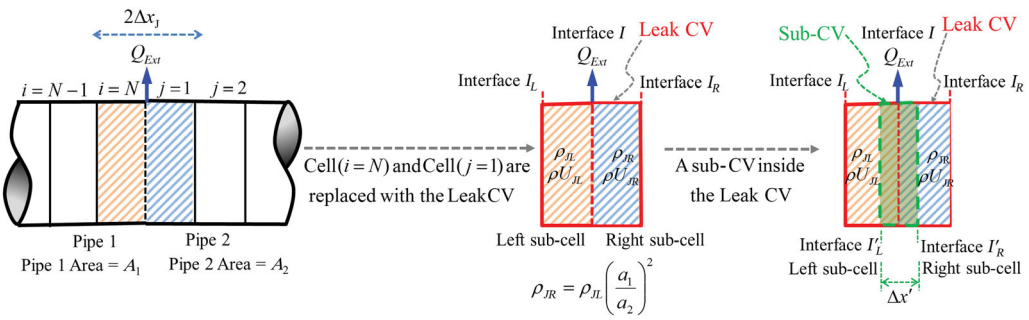

Figure 6 The discrete computation domain with junction boundary condition characterized by a flow rate discontinuity and the leak CV and the sub-CV

of the change in the wave speed magnitude across the junction. Therefore, the flow density in the left and right sub-cells becomes:

$$\rho_{JR} = \rho_{JL}\left(\frac{a_1}{a_2}\right)^2 \tag{12}$$

where a_1 is the value of wave speed in pipe 1 and a_2 is the value of wave speed in pipe 2. By invoking Eq. (12) and taking steps similar to the previous section, the mass and momentum equations for the junction CV shown in Fig. 5 become the following:

$$[\rho_{JL}]^{n+1} = [\rho_{JL}]^n + \frac{\Delta t}{\Delta x_J}\frac{1}{(A + (a_1/a_2)^2 A)}\left(\overset{\text{Mass}}{AF_{I_L}} - \overset{\text{Mass}}{AF_{I_R}}\right) \tag{13}$$

$$[\dot{m}^*]^{n+1} = [\dot{m}^*]^n + \frac{\Delta t}{2\Delta x_J}\left(\overset{\text{Mom}}{AF_{I_L}} - \overset{\text{Mom}}{AF_{I_R}}\right) \tag{14}$$

where $\dot{m}^* = \rho_{JL}U_{JL}A = \rho_{JR}U_{JR}A$. From Eqs (13) and (14), ρ_{JL} and $\dot{m}^*$ at time step $n+1$ can be computed and then used to calculate ρ_{JR}, U_{JL} and U_{JR} at time step $n+1$.

Junction boundary condition characterized by flow rate discontinuity

A change in the flow rate is commonly observed in a single pipe system due to (i) the flow from a leak (i.e. an unplanned loss of fluid), and (ii) the flow distribution (i.e. consumptive flow or conveyed flow to other parts of the pipe system). Such external flows are denoted by Q_{Ext}. Figure 6 shows a computational domain including two pipes of area A, which is uniformly discretized. The external flow takes place at an interface located between the cell $(i = N)$ and the cell $(j = 1)$. A leak CV including two sub-cells is specified such that the left sub-cell lies in cell $(i = N)$ and the right sub-cell lies in cell $(j = 1)$. The external flow is placed at the boundary interface. The boundary interface, and the left and right interfaces of the leak CV are denoted by interface I, interface $\mathrm{I_L}$ and interface $\mathrm{I_R}$, respectively. The flow variables inside the sub-cells, taken from those inside cell $(i = N)$ and cell $(j = 1)$, are distinguished by subscripts $_{\mathrm{JL}}$ and $_{\mathrm{JR}}$ for the left sub-cell and the right sub-cell, respectively (Fig. 6). The size of the leak CV is denoted by $2\Delta x_J$, assuming the size of the sub-cells is identical. In the current study, $\Delta x_J = \Delta x$.

The integral form of the mass conservation law applied to the leak CV with an orifice-type side-flow as shown in Fig. 6 gives (Nixon, 2005; Wang, Lambert, Simpson, Liggett, & Vítkovskỳ, 2002):

$$\frac{\partial}{\partial t}\int_{\mathcal{V}} \rho\, \mathrm{d}\mathcal{V} + \int_{I_L} \rho U\, \mathrm{d}A - \int_{I_R} \rho U\, \mathrm{d}A - \rho Q_{\mathrm{Ext}} = 0 \tag{15}$$

where Q_{Ext} is the external discharge. Q_{Ext} is expressed by the orifice equation below:

$$Q_{Ext} = \mathrm{sign}(H_L - H_0)\alpha\sqrt{2 \times 9.81(H_L - H_0)} + \beta \tag{16}$$

where α corresponds to both the leak size coefficient and the leak area size; β is a constant external flow rate; H_L is the instant internal pressure head; H_0 is the instant external pressure head (i.e. the atmospheric pressure); and sign function represents the direction of the flow, with $+1$ for flow in the indicated positive direction and -1 for flow in the opposite direction. The general definition of Q_{Ext} (Eq. (16)) makes it easy to investigate scenarios such as a pure leak flow (i.e. $\beta = 0$) and a lateral flow (i.e.

$\alpha = 0$). Integration of Eq. (15) from time t^n to t^{n+1} gives:

$$\left(\left[\int_{\forall} \rho \, \mathrm{d}\forall\right]^{n+1} - \left[\int_{\forall} \rho \, \mathrm{d}\forall\right]^{n}\right) - \int_{t^n}^{t^{n+1}} [\rho UA]_{I_L} \, \mathrm{d}t + \int_{t^n}^{t^{n+1}} [\rho UA]_{I_R} \, \mathrm{d}t - \rho_J Q_{Ext} \Delta t = 0 \tag{17}$$

where ρ_J is the fluid density at the side-flow interface and is approximated as follows:

$$\rho_J = \frac{\rho_{JL} + \rho_{JR}}{2} \tag{18}$$

By invoking Eq. (18), Eq. (17) becomes

$$[\rho_{JL} + \rho_{JR}]^{n+1} = [\rho_{JL} + \rho_{JR}]^{n} + \frac{1}{A\Delta x_J} \times \left(\int_{t^n}^{t^{n+1}} [\rho UA]_{I_L} \, \mathrm{d}t - \int_{t^n}^{t^{n+1}} [\rho UA]_{I_R} \, \mathrm{d}t + \frac{\rho_{JL} + \rho_{JR}}{2} Q_{Ext} \Delta t\right) \tag{19}$$

Similarly, the integral form of the momentum equation with an orifice-type external flow (Nixon, 2005; Wang et al., 2002) is applied to the leak CV as follows:

$$\frac{\partial}{\partial t} \int_{\forall} \rho U \, \mathrm{d}\forall - \int_{I_L} \rho U^2 \, \mathrm{d}A + \int_{I_R} \rho U^2 \, \mathrm{d}A - \rho U Q_{Ext} = \sum F'_x \tag{20}$$

where $\sum F'_x = (PA)_{I_L} - (PA)_{I_R}$ is the net pressure force exerted on the leak CV in x-direction. $\rho U Q_{Ext}$ in Eq. (20) is the amount of momentum flux taken out by the external discharge. The dimensionless analysis of the mass and momentum equations with an orifice-type external flow indicates that $\rho U Q_{Ext}$ is negligible (Appendix). Therefore, Eq. (20) after integrating with respect to time and space becomes:

$$[\rho_{JL} U_{JL} + \rho_{JR} U_{JR}]^{n+1} = [\rho_{JL} U_{JL} + \rho_{JR} U_{JR}]^{n} + \frac{1}{A\Delta x_J} \left(\int_{t^n}^{t^{n+1}} [\rho U^2 A + PA]_{I_L} \, \mathrm{d}t - \int_{t^n}^{t^{n+1}} [\rho U^2 A + PA]_{I_R} \, \mathrm{d}t\right) \tag{21}$$

The time-dependent integral terms in Eqs (19) and (21) are time-dependent mass and momentum fluxes multiplied by pipe area across the interfaces I_L and I_R, shown in Fig. 6. The time-dependent mass and momentum fluxes are denoted by $\overset{\text{Mass}}{F}$ and $\overset{\text{Mom}}{F}$, respectively. Therefore, Eqs (19) and (21) can be rewritten as follows:

$$\overline{\rho}^{n+1} = \overline{\rho}^{n} + \frac{1}{\Delta x_J}\left[\overset{\text{Mass}}{F}_{I_L} - \overset{\text{Mass}}{F}_{I_R}\right] - \frac{\Delta t}{2A\Delta x_J} \overline{\rho}^{n} Q^{n}_{Ext} \tag{22}$$

$$\overline{\rho U}^{n+1} = \overline{\rho U}^{n} + \frac{1}{\Delta x_J}\left\{\overset{\text{Mom}}{F}_{I_L} - \overset{\text{Mom}}{F}_{I_R}\right\} \tag{23}$$

where

$$\overline{\rho} = \rho_{JL} + \rho_{JR}, \quad \overline{\rho U} = \rho_{JL} U_{JL} + \rho_{JR} U_{JR} \tag{24}$$

From Eqs (22) and (23), $\overline{\rho}$ and $\overline{\rho U}$ are determined at time t^{n+1}. However, calculating four unknown flow variables (i.e. ρ_{JL}, U_{JL}, ρ_{JR} and U_{JR} at time t^{n+1}) is impossible using only two derived conservation equations (Eqs (22) and (23)). Therefore, two extra equations are required to preserve mass and momentum across the external flow interface. To deal with the problem, the conservation laws are additionally applied on a sub-CV of width $\Delta x'$ located between the interface I'_L and I'_R shown in Fig. 6, such that the flow variables across the sub-CV interfaces are continuous.

The mass and momentum equations applied on the sub-CV are:

$$A\frac{\Delta x'}{2}\left\{[\rho_{JL} + \rho_{JR}]^{n+1} - [\rho_{JL} + \rho_{JR}]^{n}\right\} = \int_{t^n}^{t^{n+1}} [\rho UA]_{I'_L} \, \mathrm{d}t - \int_{t^n}^{t^{n+1}} [\rho UA]_{I'_R} \, \mathrm{d}t + \frac{\rho_{JL} + \rho_{JR}}{2} Q_{Ext} \Delta t \tag{25}$$

$$A\frac{\Delta x'}{2}\left\{[\rho_{JL} U_{JL} + \rho_{JR} U_{JR}]^{n+1} - [\rho_{JL} U_{JL} + \rho_{JR} U_{JR}]^{n}\right\} = \int_{t^n}^{t^{n+1}} [\rho U^2 A + PA]_{I'_L} \, \mathrm{d}t - \int_{t^n}^{t^{n+1}} [\rho U^2 A + PA]_{I'_R} \, \mathrm{d}t \tag{26}$$

As $\Delta x'$ tends to zero, Eqs (25) and (26) become:

$$\rho_{JL} U_{JL} = \rho_{JR} U_{JR} - \frac{\rho_{JL} + \rho_{JR}}{2A} Q_{Ext} \tag{27}$$

$$a^2[\rho_{JL} - \rho_{JR}] = \rho_{JL} U^2_{JL} - \rho_{JR} U^2_{JR} \tag{28}$$

Eqs (27) and (28) are quasi-steady equations that are valid for each time step. So by invoking Eq. (24), the mass fluxes at time step $n+1$ inside the left sub-cell and the right sub-cell are then determined as follows:

$$[\rho_{JL} U_{JL}]^{n+1} = \frac{\overline{\rho U}^{n+1}}{2} - \frac{\overline{\rho}^{n+1}}{4A} Q^{n+1}_{Ext} \tag{29}$$

$$[\rho_{JR} U_{JR}]^{n+1} = \overline{\rho U}^{n+1} - [\rho_{JL} U_{JL}]^{n+1} \tag{30}$$

where

$$Q^{n+1}_{Ext} = \mathrm{sign}(H^{n+1}_{JL} - H_0)\alpha\sqrt{2g(H^{n+1}_{JL} - H_0)} + \beta, \quad H^{n+1}_{JL} = \frac{a^2 \overline{\rho}^{n+1}}{\rho_0 g}, \quad H_0 = \frac{a^2 \rho_0}{\rho_0 g} \tag{31}$$

By coupling Eqs (22), (23), (28), (29), and (30), respectively, ρ^{n+1}_{JL} is determined from the cubic polynomial equation below:

$$\theta_1(\rho^{n+1}_{JL})^3 + \theta_2(\rho^{n+1}_{JL})^2 + \theta_3(\rho^{n+1}_{JL}) + \theta_4 = 0 \tag{32}$$

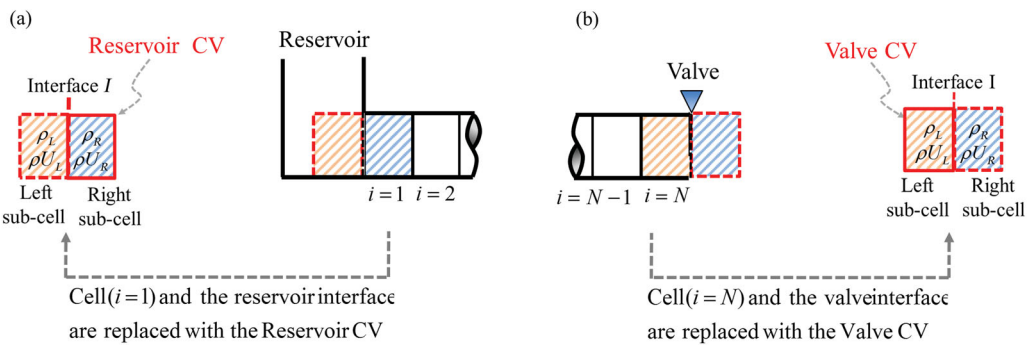

Figure 7 (a) The reservoir boundary condition. (b) The valve boundary condition

where

$$\theta_1 = -2, \quad \theta_2 = 3\overline{\rho}^{n+1}, \quad \theta_3 = \left[\frac{(\rho_{JL}U_{JL})^{n+1}}{a}\right]^2 + \left[\frac{(\rho_{JR}U_{JR})^{n+1}}{a}\right]^2 - (\overline{\rho}^{n+1})^2, \ \theta_4 = -\overline{\rho}^{n+1}\left[\frac{(\rho_{JL}U_{JL})^{n+1}}{a}\right]^2 \tag{33}$$

The coefficients of Eq. (32) (i.e. θ_1, θ_2, θ_3 and θ_4) are known from Eqs (22), (29) and (30), so ρ_{JL}^{n+1} can be obtained by explicitly solving Eq. (32). Once ρ_{JL}^{n+1} is determined, ρ_{RL}^{n+1} is calculated from Eq. (24). In short, ρ and ρU at time t^{n+1} are individually updated at the left and right sub-cells from fluid information at time t^n.

Reservoir boundary condition

Besides supplying or storing fluid, a reservoir maintains a required supply pressure for the entire downstream pipe system. Fluid is driven by gravity into the pipe system from the reservoir, which has high pressure relative to other portions of the system, to locations of lower pressure. The condition dictated by the reservoir (i.e. an upstream constant pressure) is locally imposed at the reservoir interface which is located between the reservoir and a numerical cell ($i = 1$) shown in Fig. 7a.

To treat the reservoir boundary condition, a reservoir CV, including two sub-cells, is considered. In the reservoir CV, the left and right sub-cells are denoted by subscripts $_L$ and $_R$, respectively and a cell interface separating two sub-cells is denoted by the interface I. The reservoir CV is placed such that the cell ($i = 1$) lies inside the right sub-cell shown in Fig. 7a. The left sub-cell lies inside the reservoir and is an imaginary cell. The flow variables inside the left sub-cell need to be determined while those inside the right sub-cell are adopted from cell ($i = 1$). The constant pressure (P_0) implies a constant density (ρ_0) at the reservoir interface from the state equation ($P_0 = \rho_0 a^2$), so a constant physical condition can be imposed on density rather than pressure. The mass flux in the left sub-cell is set identical to that in the right sub-cell and is, thus, mathematically speaking a transmissive boundary condition. The reservoir boundary condition is expressed in the following form:

$$\left.\frac{\partial(\rho U)}{\partial x}\right|_{\mathrm{I}} = 0 \rightarrow (\rho U)_{\mathrm{L}} = (\rho U)_{\mathrm{R}}, \qquad \rho|_{\mathrm{I}} = \rho_0 \rightarrow \rho_{\mathrm{L}} = 2\rho_0 - \rho_{\mathrm{R}} \tag{34}$$

Sudden valve closure boundary condition

In Fig. 7b, the valve is locally placed at the valve interface which is located in the right interface of cell ($i = N$). A sudden valve closure physically causes the flow rate (or the mass flux) to abruptly become zero at the valve location. To evaluate the valve boundary condition, a valve CV is specified that includes two sub-cells denoted by subscript $_L$ for the left sub-cell and subscript $_{\mathrm{R}}$ for the right sub-cell. The boundary interface located between the two sub-cells is denoted by the interface I as shown in Fig. 7b. The valve CV is placed in the numerical domain such that cell ($i = N$) lies inside the left sub-cell and the right sub-cell lies outside of the numerical domain (Fig. 7b). The right sub-cell is called an imaginary cell or a ghost cell. The flow variables inside the right sub-cell need to be determined while those inside the left sub-cell are adopted from cell ($i = N$).

A sudden valve closure imposes the zero-mass flux condition right at the valve interface (i.e. the boundary interface). Therefore, the mass flux inside the left sub-cell can be approximated from the mass flux at the right sub-cell using an extrapolation technique such that the zero-mass flux at the valve interface is met (i.e. a zero-flux boundary condition). The fluid density at the left sub-cell is held the same as that at the right sub-cell (i.e. a transmissive boundary condition). The pressure/density identity is physically implied from the classical water hammer equation when the flow velocity is zero. As linear extrapolation is used, the valve boundary condition treatment can be mathematically expressed as follows:

$$\left.\frac{\partial\rho}{\partial x}\right|_I = 0 \rightarrow \rho_R = \rho_L, \quad \rho U|_I = 0 \rightarrow (\rho U)_R = -(\rho U)_L \tag{35}$$

The same boundary treatment can be used for a partially sudden valve closure as follows:

$$\left.\frac{\partial \rho}{\partial x}\right|_I = 0 \rightarrow \rho_R = \rho_L,$$
$$\rho U|_I = \rho_{valve} U_{valve} \rightarrow (\rho U)_R = 2(\rho_{valve} U_{valve}) - (\rho U)_L \quad (36)$$

where $\rho_{valve} = \rho_R = \rho_L$; and U_{valve} is the flow velocity at the valve.

Fully open valve boundary condition

The same valve CV shown in Fig. 7b is considered for treating a fully open valve boundary condition. The fully open valve boundary condition physically results in a non-zero mass flow rate at the valve interface. Mathematically, the mass flow rate inside the right sub-cell can be approximated from that inside the left sub-cell such that the mass flow rate at the valve interface is held at a non-zero constant value. The fluid density at the right sub-cell is as same as that at the left sub-cell (i.e. a transmissive boundary condition). Using a linear extrapolation, the fully open valve boundary conditions become:

$$\left.\frac{\partial \rho}{\partial x}\right|_I = 0 \rightarrow \rho_R = \rho_L,$$
$$\rho UA|_I = \dot{m}_{valve} \rightarrow (\rho UA)_R = 2\dot{m}_{valve} - (\rho UA)_L \quad (37)$$

where $\dot{m}_{valve}$ is the mass flow rate at the valve.

Reservoir and valve boundary conditions may also be conceptualized as junctions characterized by a geometric discontinuity. A reservoir may be thought of as a junction where a pipe of fixed diameter connects to another pipe whose diameter tends to infinity. A valve may be viewed as a junction where a pipe of diameter D_1 connects to another pipe whose diameter may vary from D_1 (i.e. fully open valve) to 0 (i.e. fully closed valve).

4 Numerical results validation and discussions

The objective of this section is to investigate the properties of the proposed unified finite volume schemes, i.e. the accuracy and efficiency of the schemes (Hirsch, 2007), under different flow conditions. To achieve this goal, three numerical test cases involving different boundary conditions are designed. Through these test cases, the ability of the proposed schemes to capture water hammer wave interactions with a junction is investigated. Table 1 represents the relevant flow features for each numerical test case.

The analysis of the proposed framework is conducted through comparison with the analytical solution, and solution of fixed-grid MOC with linear space-line interpolation (Ghidaoui & Karney, 1994; Ghidaoui, Karney, & McInnis, 1998). The numerical dissipation is quantitatively measured using (i) the integrated energy method denoted by ξ_E (Karney, 1990), and (ii) the L^2-norm method denoted by ξ_{L^2} (Chaudhry & Hussaini, 1985; Ghidaoui et al., 2005).

In the next section, the accuracy and efficiency of the KFVS and BGK schemes are investigated for each test case. Note that all fluxes at boundary interfaces are approximated by 1st-order mesoscopic-based models.

Table 1 Numerical test cases[a]

Test no.	Flow feature
1	Wave interaction with a junction characterized by a geometric discontinuity
2	Wave interaction with a junction characterized by a discontinuity in the value of wave speed
3	Wave interaction with a junction characterized by a flow rate discontinuity

[a] The discontinuous wave is evoked by a sudden valve closure of the downstream valve.

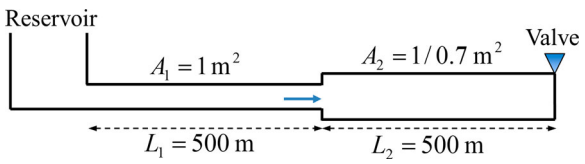

Figure 8 The system configuration for test case 1

Table 2 Geometric and hydraulic parameters for test case 1[a]

Pipe no.	L (m)	a (ms^{-1})	A (m^2)
Pipe 1	500	1000	1
Pipe 2	500	1000	1/0.7

[a] The discontinuous wave is evoked by a sudden valve closure of the downstream valve. The initial mass flow rate (i.e. $\dot{m}_0$) in pipe 1 and pipe 2 is 1285.7 kgs^{-1} where the initial density is 1000 kgm^{-3}.

4.1 *Test case 1: wave interaction with a junction characterized by a geometric discontinuity*

Test case 1, shown in Fig. 8, includes two pipes in series connected to an upstream reservoir and a downstream valve (i.e. a reservoir-pipes-valve configuration). At the location where the two pipes are joined (i.e. the junction) the cross-sectional area abruptly changes. A transient is generated by a sudden closure of the downstream valve. Test case 1 is designed to investigate how well the mesoscopic-based schemes using the proposed boundary condition can simulate the wave interaction with the junction where the pipe cross-sectional area abruptly changes. The value of wave speed is $a = 1000\,\mathrm{ms}^{-1}$ for both pipes. In addition, wall friction and local losses at the junction are neglected; thus, any observed dissipation in results will be purely numerical. Relevant geometric and hydraulic parameters for test case 1 are given in Table 2.

KFVS scheme

The initial conditions (i.e. flow velocity and fluid density at time $t = 0$) cannot be easily determined for the proposed mesoscopic-based schemes which are fully compressible. One alternative to obtain steady state variables is to apply the unsteady model to

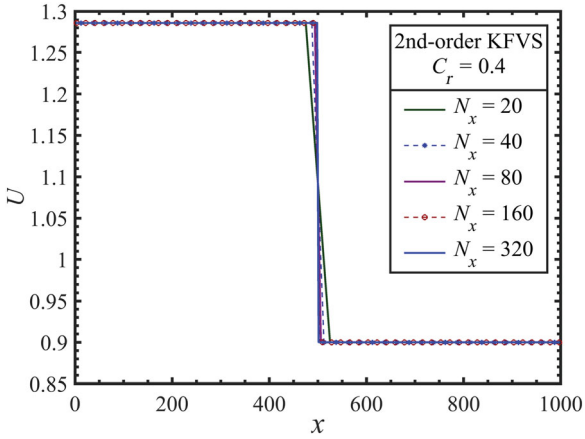

Figure 9 Velocity before the valve sudden closure produced by 2nd-order KFVS (test case 1)

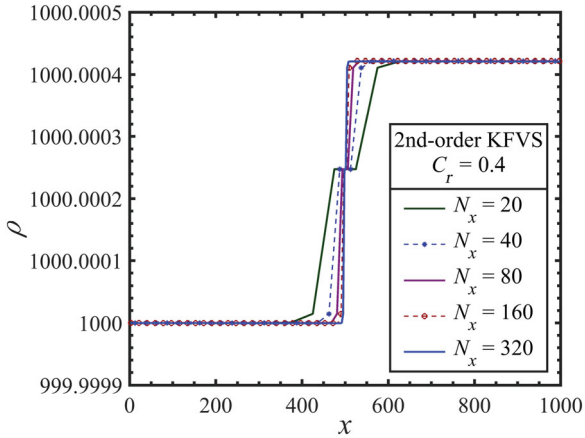

Figure 10 Density before the valve sudden closure produced by 2nd-order KFVS (test case 1)

the system shown in Fig. 8, where the valve is fully open and pressure head at the reservoir is constant, i.e. a time-marching approach (Hirsch, 2007). The velocity and density in the entire computational domain before valve closure at the steady state, then, are achieved and shown in Figs 9 and 10. The converged solution serves as the initial condition for the problem in which the transient is induced by a sudden valve closure.

Figure 11 shows that the transient solutions produced by the 2nd-order KFVS scheme tend to the exact solution (i.e. the black dashed-line in Fig. 11) as the grid size tends to zero. The initial conditions are adopted from the steady model (Figs 9 and 10). The highly dissipative nature of the KFVS schemes dominates the local/minor errors. Thus, in the next section the BGK scheme is implemented for test case 1.

BGK scheme

Figure 12 shows the steady fluid density obtained using the BGK scheme when the grid number (i.e. N_x) is less than or equal to 160. The steady state solution is flawless at the pipes' internal sections, but oscillatory just before and after the junction cell. The oscillations, whose amplitudes are small, violate the stability criterion of the steady model when the grid number is more

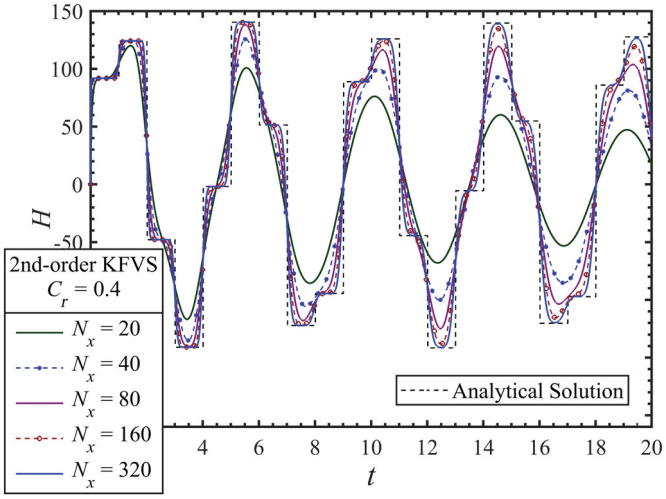

Figure 11 Pressure head traces at the valve produced by 2nd-order KFVS (test case 1)

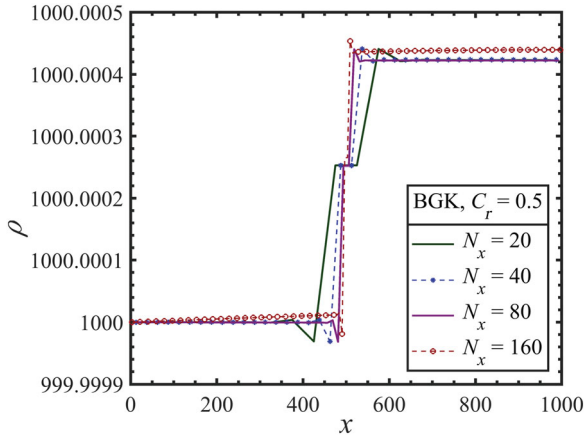

Figure 12 Fluid density before the valve sudden closure produced by BGK (test case 1)

than 160. For example, when $N_x = 320$, a steady state solution cannot be achieved.

The oscillations, which appear to be unaffected by the grid size, can be resolved if the collision time expression, proposed by Xu (1998) and modified by Mesgari Sohani and Ghidaoui (2018), takes into account the discontinuity of the cross-sectional area besides the discontinuity in flow variables. New forms for the collision time at the interface $x_{i=N-1/2}$ in pipe 1 and the interface $x_{j=3/2}$ in pipe 2 are proposed to treat the junction characterized by a geometric discontinuity as follows:

$$\begin{cases} \tau_{i=N-1/2} = C_1 \dfrac{\mu_{i=N-1/2}}{p_{i=N-1/2}} \\ +C_3 \dfrac{|\rho_{i=N-1}U_{i=N-1}| - |\rho_{j=1}U_{j=1}|}{|\rho_{i=N-1}U_{i=N-1}| + |\rho_{j=1}U_{j=1}|}\Delta t & \text{in pipe 1} \\ \tau_{j=3/2} = C_1 \dfrac{\mu_{j=3/2}}{p_{j=3/2}} \\ +C_3 \dfrac{|\rho_{i=N}U_{i=N}| - |\rho_{j=2}U_{j=2}|}{|\rho_{i=N}U_{i=N}| + |\rho_{j=2}U_{j=2}|}\Delta t & \text{in pipe 2} \end{cases} \tag{38}$$

where i and j are the index number in pipe 1 and pipe 2, respectively; N is the number of grid cells in pipe 1; and C_1 and C_3

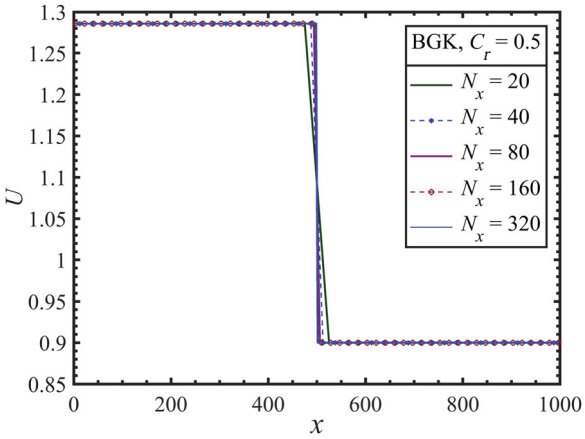

Figure 13 Velocity before the valve sudden closure produced by BGK with the modified collision term (test case 1)

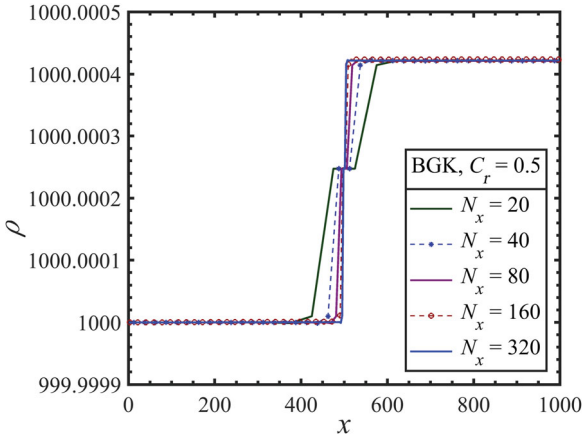

Figure 14 Density before the valve sudden closure produced by BGK with the modified collision term (test case 1)

are constants and determined from numerical experimentations. The modified numerical terms in Eq. (38) (i.e. the second terms in the right-hand side of Eq. (38)) determine the collision time by coupling the flow variables of the last cell in pipe 1 and those of the first cell of pipe 2. For the computational experimentation, oscillation-free results are achieved when C_1 and C_3 are set to 1.0 and 10.0, respectively. The obtained steady state solutions produced by the BGK scheme with the modified collision time (Eq. (38)) are shown in Figs 13 and 14.

Figure 15 presents the pressure head traces at the valve produced by the BGK scheme for $C_r = 0.5$. In the BGK scheme, the collision time is calculated from Eq. (38) around the junction and the initial conditions are adopted from the achieved steady state shown in Figs 13 and 14. The results shown in Fig. 15 converge to the analytical solution as Δx and Δt tend to zero. However, slight local discrepancies are observed at $t = 8$ s, $t = 10$ s, $t = 17$ s, and $t = 19$ s in Fig. 15. As the grid size is reduced, the amplitude of the discrepancies reduces but does not vanish (see the magnified region in Fig. 15). The origin of the discrepancies is a local energy dissipation (h_{loss}) at steady state imposed by the junction boundary treatment (Eqs (8) and (10)). To illustrate how the local energy dissipation at the junction is

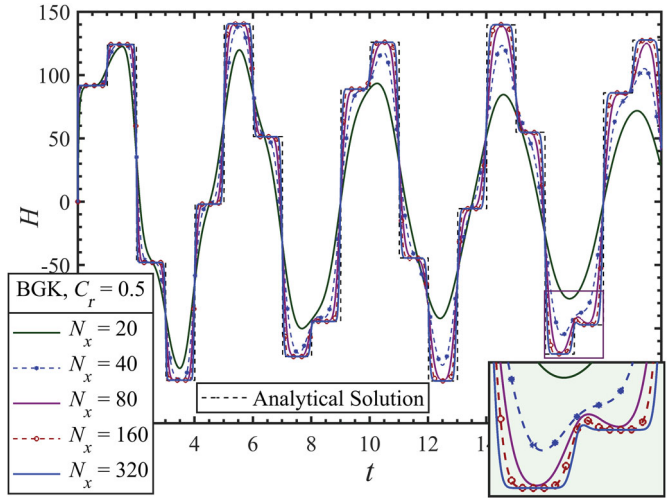

Figure 15 Pressure head traces at the valve produced by BGK with the modified collision term (test case 1)

included in the boundary formulation, the mass and momentum conservation laws are formulated at the junction where pipe 1 and pipe 2 are connected as follows:

$$U_1 A_1 = U_2 A_2 \tag{39}$$

$$\rho A_2 U_2^2 - \rho A_1 U_1^2 = P_1 A_1 + P'(A_2 - A_1) - P_2 A_2 \tag{40}$$

where P' is the pressure acting on the vertical wall of the junction (i.e. $A_2 - A_1$). It is found that $P_1 \cong P'$ for the small radial acceleration at the junction. From Eqs (39) and (40), the energy equation at the junction is derived as follows:

$$\frac{P_1}{9.81\rho} + \frac{U_1^2}{2 \times 9.81} = \frac{P_2}{9.81\rho} + \frac{U_2^2}{2 \times 9.81} + h_{loss} \tag{41}$$

where

$$h_{loss} = \frac{U_2^2}{2 \times 9.81} + \frac{U_1^2}{2 \times 9.81} - \frac{U_1 U_2}{9.81} \tag{42}$$

In Eq. (42), h_{loss} is the pressure head loss (i.e. the local energy dissipation) at the junction. h_{loss} is physically described by eddy motion formation near the junction. Such a local dissipation mechanism is also observed in the hydraulic jump, as discussed by Abbott (1979).

Comparison of the mesoscopic-based schemes

Figure 16 represents the head traces produced by the mesoscopic-based schemes for $N_x = 320$. In spite of the highly dissipative nature of the KFVS schemes, they reproduce the correct form of the transient waves, particularly during the first wave cycle. In addition, E/E_0 for different schemes is given in Fig. 17 for $N_x = 320$, where E is the total energy (i.e. the sum of kinetic and internal energy) in the pipe proposed by Karney (1990). In the pipe, the velocity and, thus, the work at the valve are zero. In addition, the pressure wave and, thus, the work

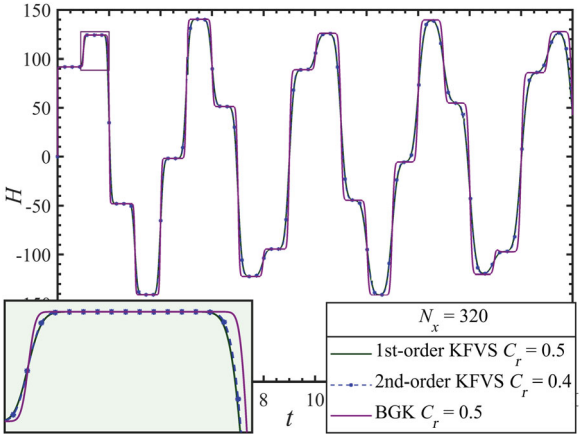

Figure 16 Pressure head traces at the valve produced by the mesoscopic-based schemes for $N_x = 320$ (test case 1)

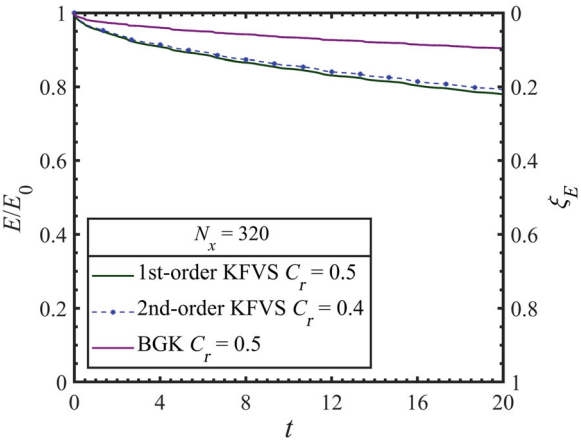

Figure 17 Energy head traces for the mesoscopic-based schemes when $N_x = 320$ (test case 1)

at the reservoir are zero. Moreover, the friction and, thus, the energy dissipation are zero. As result, the total energy is invariant with time: $E/E_0 = 1$, where E_0 is the total energy before any disturbance. Thus, any deviation of E/E_0 from 1 is due to numerical dissipations. ξ_E, shown in Fig. 17, indicates the errors calculated from the integral energy equation as follows:

$$\xi_E = 1 - \frac{E}{E_0} \tag{43}$$

The numerical errors are measured from the energy equation of Karney (1990) (i.e. ξ_E) and the L^2-norm method (i.e. ξ_{L^2}) as the functions of the number of grids and are shown in Figs 18 and 19, respectively.

For test case 1, the computational time required to reach the steady state solution denoted t_{steady} are reported in Table 3. From the results of numerical experimentations, it is observed that mesoscopic-based schemes require more time steps to reach a steady state as the grid cell size is reduced. For the BGK scheme, the required convergence time is enormously large when $N_x = 320$. The poor convergence of the BGK scheme to steady state, as reported by Xu (1998), is due to time-dependent fluxes of the

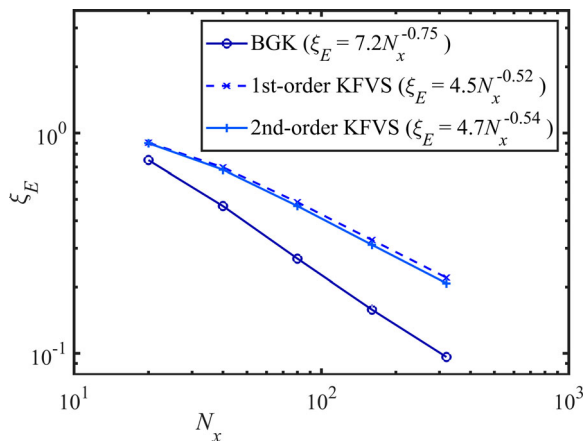

Figure 18 ξ_E versus the number of grids (test case 1)

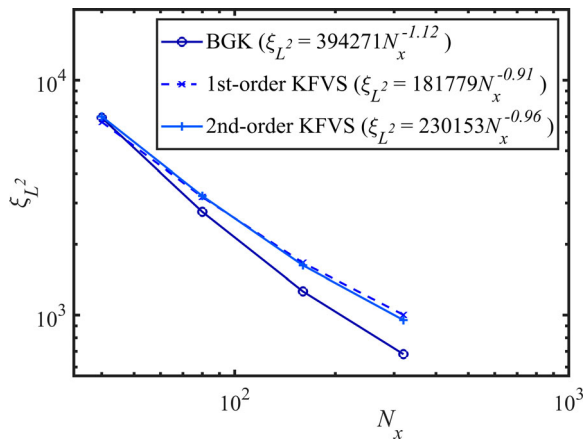

Figure 19 ξ_{L^2} versus the number of grids (test case 1)

BGK scheme. For the steady state calculation Xu (1998) suggested that the relaxation process must be simplified in order to yield time independent numerical fluxes. Testing the assertion of Xu (1998) will be left to a future study.

4.2 *Test case 2: wave interaction with a junction characterized by a discontinuity in the value of wave speed*

Figure 20 depicts the system configuration for test case 2, which includes two pipe segments in series connected to an upstream reservoir and a downstream valve. The material and thickness of pipe 1 are different from those of pipe 2, resulting in a change of wave speed across the junction joining the two pipes. To evaluate the effect of a discontinuity in wave speed, the flow inside the pipe is subjected to a severe transient due to sudden closure of the downstream valve. Test case 2 is designed to investigate the capability of the mesoscopic-based schemes to simulate transients when the value of the wave speed changes abruptly.

The relevant geometric and hydraulic parameters for the numerical test case 2 are provided in Table 4. Wall friction and local losses at the junction are neglected so any dissipation observed will be purely numerical. In this way, numerical dissipation can be quantified.

Table 3 Converging time t_{steady} for test case 1

N_x	1st-KFVS scheme ($C_r = 0.5$)		2nd-KFVS scheme ($C_r = 0.4$)		BGK scheme ($C_r = 0.5$)	
	t_{steady} (s)	Δt (s)	t_{steady} (s)	Δt (s)	t_{steady} (s)	Δt (s)
20	400	0.025	400	0.02	400	0.025
40	400	0.0125	400	0.01	400	0.0125
80	400	0.00625	400	0.005	400	0.00625
160	400	0.003125	400	0.0025	800	0.003125
320	600	0.0015625	600	0.00125	20,000	0.0015625

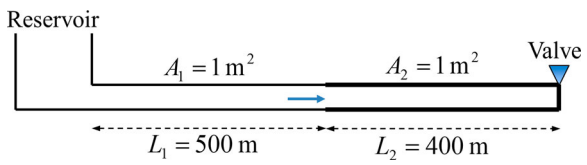

Figure 20 The system configuration for test case 2

Table 4 Geometric and hydraulic parameters for test case 2[a]

Pipe no.	L (m)	a (ms^{-1})	A (m^2)
Pipe 1	500	1000	1
Pipe 2	400	800	1

[a] The discontinuous wave is evoked by a sudden valve closure of the downstream valve. The initial mass flow rate (i.e. $\dot{m}_0$) in pipe 1 and pipe 2 is 900 kgs^{-1} where the initial density is 1000 kgm^{-3}.

Similar to test case 1, both steady and unsteady models are required in order to investigate transient behaviours. This test scenario uses the reservoir-pipe-valve system shown in Fig. 20, where the valve is fully opened and pressure head at the reservoir is constant. In the unsteady models, the same discrete time-dependent model is used such that the converged flow variables serve as the initial condition and the transient is initiated by a sudden valve closure. The numerical results obtained from the steady model and the unsteady model are discussed separately in the next section.

The steady model

The converged flow variables for test case 2 produced by the 1st-order KFVS are shown in Figs 21 and 22. The state flow variables obtained from the 2nd-order KFVS and BGK schemes are similar to those variables produced by the 1st-order KFVS scheme.

The proposed compressible models cause a sharp change of fluid density across the pipe junction (Fig. 22). To investigate why the proposed models impose such a large, unrealistic density in the steady state, the conservation equations of mass and momentum are applied at the junction, where pipe 1 and pipe 2 are connected, as follows:

$$U_1\rho_1 = U_2\rho_2 \tag{44}$$

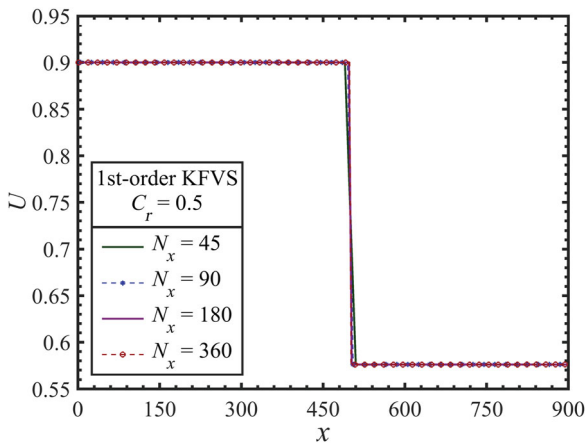

Figure 21 Velocity before the valve sudden closure produced by 1st-order KFVS (test case 2)

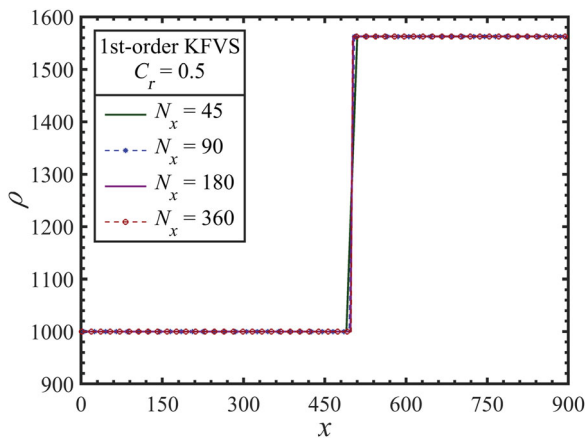

Figure 22 Density before the valve sudden closure produced by 1st-order KFVS (test case 2)

$$\rho_2 U_2^2 - \rho_1 U_1^2 = P_1 - P_2 \tag{45}$$

Starting from the mass and momentum conservation equations (Eqs (44) and (45)), the energy equation associated with the flow inside the pipes is obtained below:

$$\frac{P_1}{9.81\rho_1} + \frac{U_1^2}{2 \times 9.81} = \frac{P_2}{9.81\rho_2} + \frac{U_2^2}{2 \times 9.81} + \Delta H \tag{46}$$

where

$$\Delta H = \left(\frac{U_1}{U_2} - 1\right)\frac{a_2^2}{9.81} - \frac{(U_2 - U_1)^2}{2 \times 9.81} \tag{47}$$

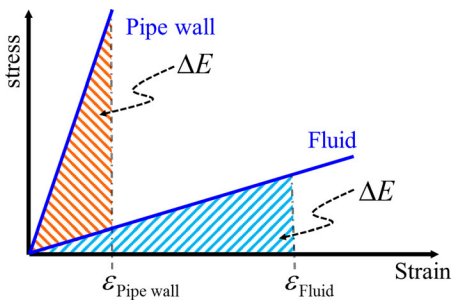

Figure 23 Stress–strain curves for pipe wall and fluid

In Eq. (47), ΔH is the energy (head) difference between two pipes. The second term in the right hand-side of Eq. (47) is negligible. In addition, the momentum equation (Eq. (45)) implies $U_2/U_1 \cong a_2^2/a_1^2$. Thus, Eq. (47) becomes:

$$\Delta H \cong \frac{(a_2 + a_1)(a_2 - a_1)}{9.81} \tag{48}$$

ΔH is considerably large, and so is the corresponding ΔE. The large energy difference in two pipes is mainly because the current mesoscopic-based models solve fluid itself in pipes and exclude any interaction between fluid and pipe wall, so fluid in pipe 1 and pipe 2 stores the total energy. However, in a realistic flow-pipe system, part of the total energy is taken by the fluid and the remainder is taken by the pipe wall. Therefore, for the case of two pipes in series, with no losses, the energy equation is represented as follows:

$$E_{fluid\ pipe1} + E_{wall\ pipe1} = E_{fluid\ pipe2} + E_{wall\ pipe2} \tag{49}$$

Consider the case in which pipe 1 is more rigid than pipe 2 (i.e. $a_1 > a_2$). Hence, for the same deformation, the proportion of energy taken by the wall of pipe 1 is larger than that taken by the wall of pipe 2. Thus, the energy stored in the fluid of pipe 2 is larger than that in the fluid of pipe 1. Therefore, the energy equation associated with the fluid itself becomes:

$$E_{fluid\ pipe2} - E_{fluid\ pipe1} = \Delta E \tag{50}$$

where ΔE is the difference between $E_{wall\ pipe1}$ and $E_{wall\ pipe2}$ and is quantitatively similar to the corresponding ΔE obtained from Eq. (48). While ΔE taken by the pipe wall results in a relatively small strain in the pipe wall (i.e. $\epsilon_{pipe\ wall}$), the same proportion of energy taken by fluid induces a large strain (i.e. ϵ_{fluid}). This is illustrated in Fig. 23 where the stress–strain curves corresponding to both the pipe wall and fluid are plotted. The hatched areas under both curves are quantitatively represent ΔE.

Even though such an extreme partitioning of energy in the steady state solution is observed in the numerical model at steady state, the net pressure in the unsteady model gives quite reasonable numerical results. The unsteady results are discussed in the next section.

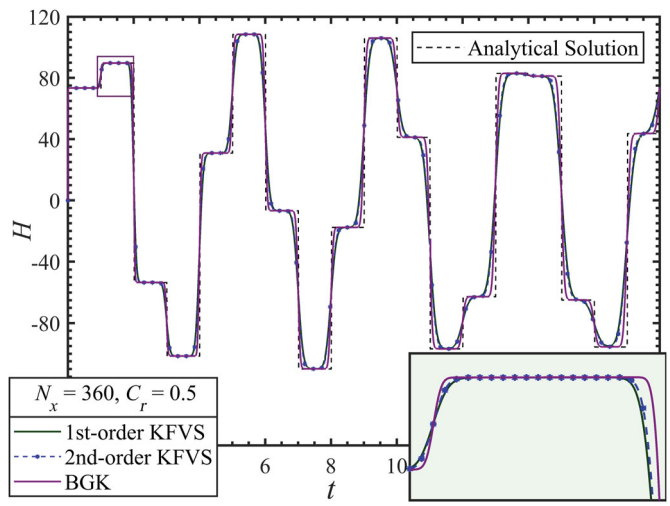

Figure 24 Pressure head traces at the valve for $N_x = 360$ (test case 2)

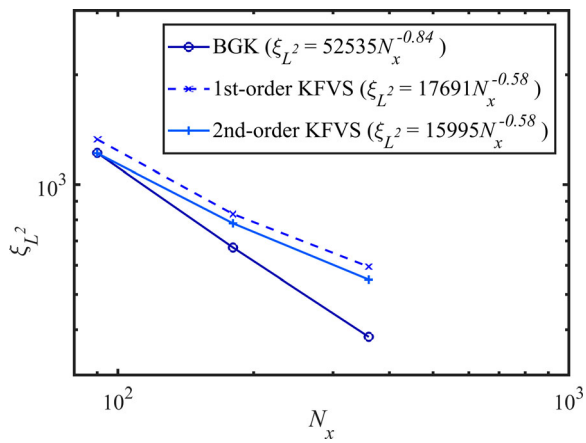

Figure 25 ξ_{L^2} versus the number of grid (test case 2)

The unsteady model

Figure 24 show the pressure head traces at the valve produced by the 1st-order KFVS scheme, the 2nd-order KFVS scheme, and the BGK scheme, respectively when $C_r = 0.5$.

Figure 24 is produced to compare the numerical results produced by the mesoscopic-based schemes when $C_r = 0.5$ and $N_x = 320$. The relation between the ξ_{L^2} and the number of grids, shown in Fig. 25, indicates that the convergence rate of the BGK scheme is significantly larger than that of the KFVS schemes.

4.3 *Test case 3: wave interaction with a junction characterized by a flow rate discontinuity*

Figure 26 shows a reservoir-pipe-valve configuration for test case 3. The pipe is connected to an upstream reservoir and a downstream valve. An external flow (i.e. Q_{Ext}) takes place in the middle of the pipe. A transient flow inside the pipe is induced by the sudden closing of the downstream valve. Test case 3 is used to study the capability of the mesoscopic-based scheme to capture the wave interaction with an external flow. The relevant geometric and hydraulic parameters for numerical test case 3 are given in Table 5.

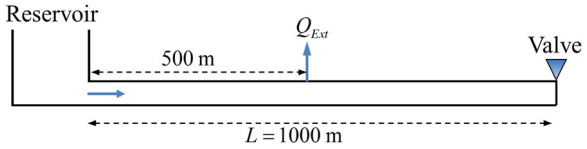

Figure 26 The system configuration for test case 3

Table 5 Geometric and hydraulic parameters for test case 3[a]

Pipe no.	L (m)	a (ms^{-1})	A (m^2)
Pipe 1	1000	1000	0.9

[a] The discontinuous wave is evoked by a sudden valve closure of the downstream valve. The initial mass flow rate (i.e. $\dot{m}_0$) driven by the reservoir inside pipe 1 is 900 kgs^{-1} where the initial density is 1000 kgm^{-3}.

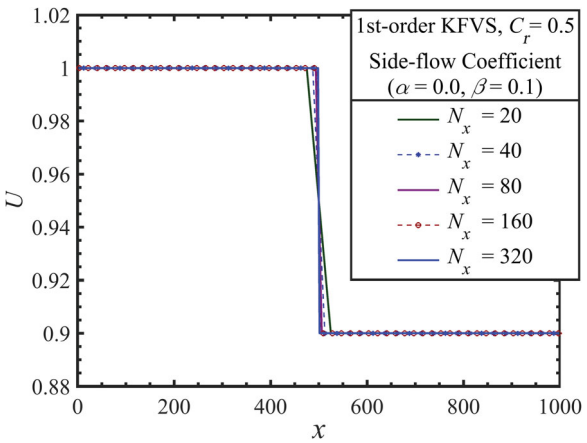

Figure 27 Velocity before the valve sudden closure (test case 3 - scenario 1)

Similar to the previous test cases, both the steady and unsteady models of compressible fluids are needed. Apart from replacing the junction boundary characterized by a change in wave speed by one characterized by a discontinuity in flow rate, the other boundary conditions imposed for test case 3 are similar to those for test case 2. Numerical experiments using the 1st-order KFVS scheme are carried out and presented for test case 3 in the next section.

1st-order KFVS scheme

Transient properties in a single pipe are affected by the amount of the external flow. Therefore, to investigate how a transient wave interacts with an arbitrary external flow, three scenarios are proposed for the coefficient of the external flow (Eq. (16)) as follows:

Scenario 1: $\alpha = 0.0\,\mathrm{m}^2$ and $\beta = 0.1\,\mathrm{m}^3\,\mathrm{s}^{-1}$
Scenario 2: $\alpha = 0.0003\,\mathrm{m}^2$ and $\beta = 0.0\,\mathrm{m}^3\,\mathrm{s}^{-1}$
Scenario 3: $\alpha = 0.0003\,\mathrm{m}^2$ and $\beta = 0.1\,\mathrm{m}^3\,\mathrm{s}^{-1}$

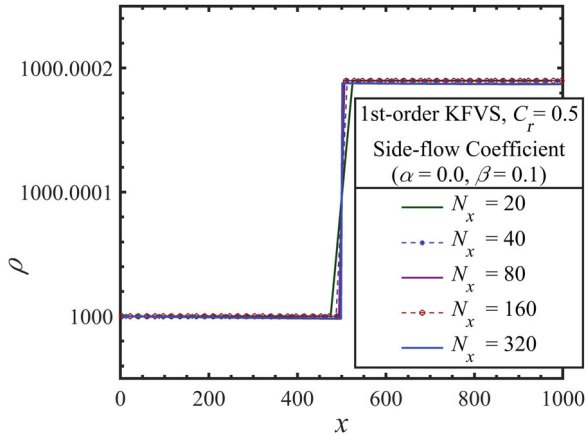

Figure 28 Density before the valve sudden closure (test case 3 - scenario 1)

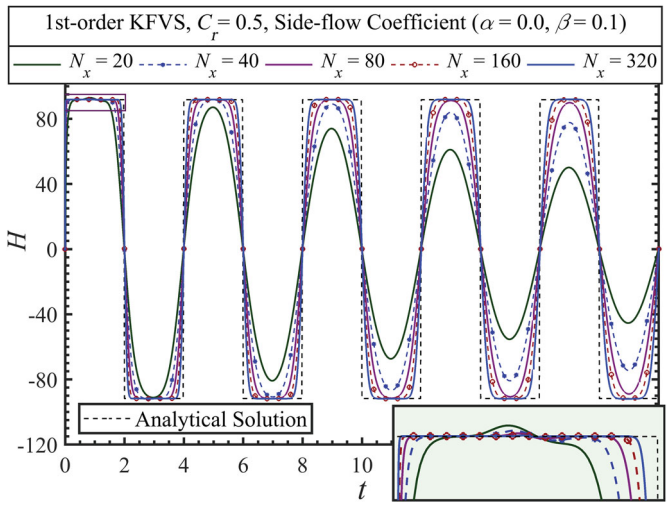

Figure 29 Pressure head traces at the valve (test case 3 - scenario 1)

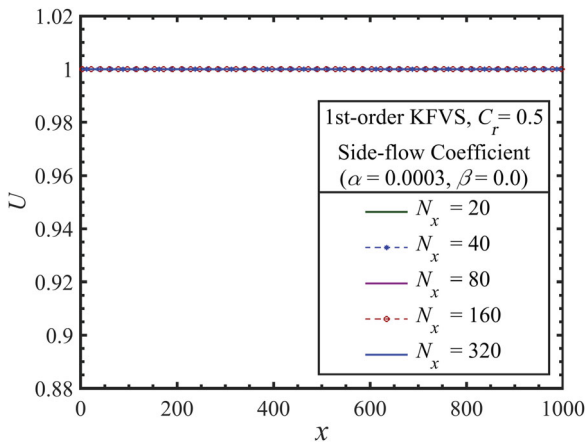

Figure 30 Velocity before the valve sudden closure (test case 3 - scenario 2)

Figures 27–35 show the converged steady state solutions and transient solutions corresponding to each scenario. In all scenarios the numerical solutions converge to the analytical solutions when $\Delta x \to 0$, $\Delta t \to 0$, and $\Delta x_J \to 0$. The numerical results

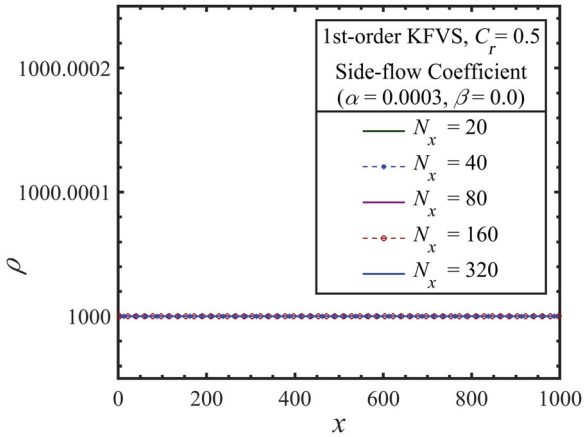

Figure 31 Density before the valve sudden closure (test case 3 - scenario 2)

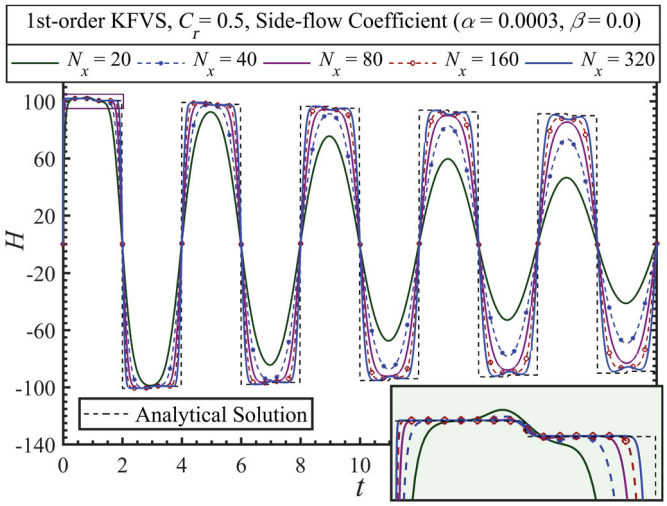

Figure 32 Pressure head traces at the valve (test case 3 - scenario 2)

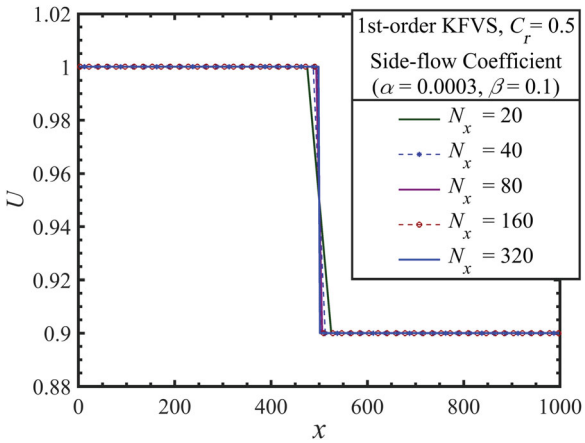

Figure 33 Velocity before the valve sudden closure (test case 3 - scenario 3)

produced by the 1st-order KFVS scheme are highly dissipative, but still correctly capture the wave in the first period (see the magnified region in Figs 29, 32, and 35). Implementation of the BGK scheme is recommended for problems where less numerical dissipation is required.

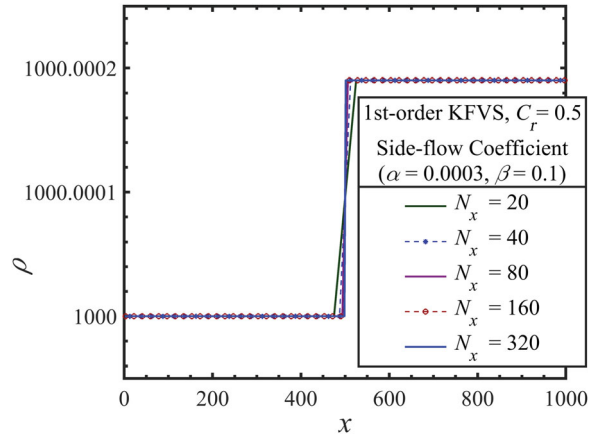

Figure 34 Density before the valve sudden closure (test case 3 - scenario 3)

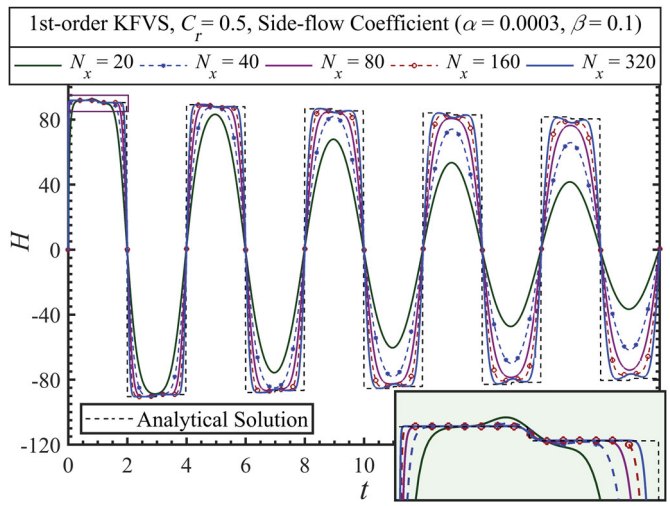

Figure 35 Pressure head traces at the valve (test case 3 - scenario 3)

5 Conclusion

This study is motivated by the need for pure FV numerical models suitable for water hammer flows. The objective is achieved by establishing a FV framework for handling boundary conditions and developing mesoscopic methods for water hammer. In the FV approach, boundary elements are formulated using the laws of mass and momentum for a control volume involving the underlying physics of hydraulics. The key results are listed as follows:

- The pure FV formulation guarantees that mass and momentum are conserved while the conservation of energy is automatically guaranteed. This formulation correctly captures discontinuity fronts and wave interactions with boundary elements.
- Stability of the proposed FV schemes is satisfied when $C_r < 0.5$. The restriction on C_r is mainly due to the kinetic approach where not only the mean velocity plays a role in the stability condition, but also particles velocities, which range from $-\infty$ to $+\infty$, contribute to the stability.

- The non-iterative boundary treatment for sudden valve closure, fully open valve, reservoir, and junction boundary conditions are successfully formulated.

Traditionally, FV solutions are designed with the premise that there is a set of governing equations that are solved throughout the flow domain together with simple boundary conditions, such as zero velocities normal and tangential to a wall. Such schemes are not readily applicable to open and closed conduits where the boundaries are more complex and often dynamic. This paper is a first attempt at showing that it is possible to design a consistent FV scheme for pipe flows by applying the laws of mass and momentum to a control volume that contains the boundary elements. Future work needs to be carried out to generalize the proposed framework to a wider range of devices and discontinuities in closed/open conduit applications.

Appendix. Derivation of one-dimensional equations for a transient flow with an orifice-type external flow

To derive the unsteady flow equations (i.e. mass and momentum equations) in a rigid pipe with a external flow, a control volume between $x = x_1$ and $x = x_2$, shown in Fig. A1, is considered. The derivation closely follows the derivation of Wang et al. (2002). The pipe is assumed to be horizontal and frictionless with an external flow located in $x = x_L$ as shown in Fig. A1, where Q_{Ext} is the external flow rate (Eq. (16)).

The conservation of mass in the control volume gives:

$$\frac{\partial}{\partial t}\int_{x_1}^{x_2}(\rho A)\,\mathrm{d}x + \int_{x_1}\rho U\,\mathrm{d}A - \int_{x_2}\rho U\,\mathrm{d}A = -\rho Q_{Ext} \tag{A1}$$

where x is the distance along the pipe; t is the time; ρ is the fluid density; A is the pipe cross-sectional area; U is the average velocity in x-direction; and Q_{Ext} is the external flow rate. The integral terms in Eq. (A1) can be simplified as:

$$\frac{\partial(\rho A)}{\partial t}\Delta x + (\rho UA)_{x_2} - (\rho UA)_{x_1} = -\rho Q_{Ext} \tag{A2}$$

where Δx is the horizontal distance between $x = x_1$ and $x = x_2$; and the last two terms in the left hand-side of Eq. (A2) are the mass fluxes at $x = x_1$ and $x = x_2$. Dividing Eq. (A2) by Δx and letting Δx approach zero gives:

$$\frac{\partial(\rho)}{\partial t} + \frac{\partial(\rho U)}{\partial x} + \frac{\rho Q_{Ext}\delta(x - x_L)}{A} = 0 \tag{A3}$$

where δ is the Dirac delta function (Nixon, 2005; Wang et al., 2002) and is defined:

$$\delta(x - x_L) = \begin{cases}\infty & \text{if } x = x_L \\ 0 & \text{otherwise}\end{cases}, \quad \lim_{\psi\to\infty}\int_{x_L-\psi}^{x_L+\psi}\delta(x - x_L)\,\mathrm{d}x = 1 \tag{A4}$$

where ψ is a small distance on the either side of the leak. Similarly, conservation of momentum in the control volume gives:

$$\frac{\partial}{\partial t}\int_{x_1}^{x_2}(\rho UA)\,\mathrm{d}x + \int_{x_1}\rho U^2\,\mathrm{d}A + \int_{x_2}\rho U^2\,\mathrm{d}A + (PA)_{x_2} - (PA)_{x_1} - \rho UQ_{Ext} = 0 \tag{A5}$$

where P is pressure. After simplification of the integral terms, Eq. (A5) becomes:

$$\frac{\partial(\rho UA)}{\partial t}\Delta x + (\rho U^2A + PA)_{x_2} - (\rho U^2A + PA)_{x_1} - \rho UQ_{Ext} = 0 \tag{A6}$$

After dividing Eq. (A6) by Δx, Eq. (A6) as Δx tends to zero gives:

$$\frac{\partial(\rho U)}{\partial t} + \frac{\partial(\rho U^2 + P)}{\partial x} - \frac{\rho UQ_{Ext}\delta(x - x_L)}{A} = 0 \tag{A7}$$

The external flow rate (Eq. (16)) is:

$$Q_{Ext} = \mathrm{sign}(H_L - H_0)\alpha\sqrt{2 \times 9.81(H_L - H_0)} + \beta \tag{A8}$$

Equations (A3), (A7) and (A8) govern the unsteady flow inside a rigid pipe with an external flow such that the state equation is $\partial P/\partial\rho = a^2$, where a is wave speed. To non-dimensionalize Eqs (A3), (A7) and (A8), the following dimensionless quantities are used:

$$P^* = \frac{P}{P_0}, \quad \rho^* = \frac{\rho}{\rho_0}, \quad t^* = \frac{t}{L/a}, \quad x^* = \frac{x}{L},$$
$$U^* = \frac{U}{U_0}, \quad Q^*_{\mathrm{Ext}} = \frac{Q_{Ext}}{Q_{Ext_0}}, \quad \delta(x^* - x^*_{\mathrm{L}}) = \delta(x - x_{\mathrm{L}})L \tag{A9}$$

where P_0 is the reference pressure; ρ_0 is the reference fluid density; L is the pipe length; a is the wave speed; Q_{Ext_0} is the reference external flow rate and U_0 is the reference flow rate. Applying the dimensionless quantities (Eqs (A9), Eqs (A3) and (A7) become:

$$\frac{\partial P^*}{\partial t^*} + \frac{U_0}{a}U^*\frac{\partial P^*}{\partial x^*} + \frac{\rho_0U_0a}{P_0}\rho^*\frac{\partial U^*}{\partial x^*} + \frac{a\rho_0Q_{Ext_0}}{AP_0}\rho^*Q^*_{Ext}\delta(x^* - x^*_L) = 0 \tag{A10}$$

$$\frac{\partial\rho^*U^*}{\partial t^*} + \frac{U_0}{a}\frac{\partial\rho^*U^{*2}}{\partial x^*} + \frac{a}{U_0}\frac{\partial\rho^*}{\partial x^*} + -\frac{U_0}{a}\frac{Q_{Ext_0}}{AU_0}U^*\rho^*Q^*_{Ext}\delta(x^* - x^*_L) = 0 \tag{A11}$$

Because U_0/a is normally so small in water hammer application, the second term in Eq. (A10) and the second and last terms in

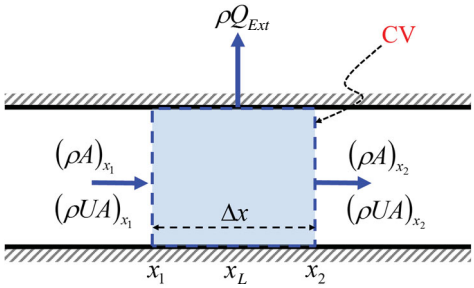

Figure A1 A pipe section with an external flow

Eq. (A11) can be neglected. Therefore, Eqs (A10) and (A11) become:

$$\frac{\partial P^*}{\partial t^*} + \frac{\rho_0 U_0 a}{P_0}\rho^* \frac{\partial U^*}{\partial x^*} + \frac{\rho_0 Q_{\mathrm{Ext}_0} a}{A P_0}\rho^* Q^*_{\mathrm{Ext}}\delta(x^* - x^*_{\mathrm{L}}) = 0 \tag{A12}$$

$$\frac{\partial \rho^* U^*}{\partial t^*} + \frac{a}{U_0}\frac{\partial \rho^*}{\partial x^*} = 0 \tag{A13}$$

Notation

A	=	area (m^2)
a	=	transient wave speed ($m\,s^{-1}$)
C_r	=	Courant number (–)
E	=	sum of total kinetic energy and total internal energy (J)
$\boldsymbol{F}$	=	numerical time-dependent fluxes along x-direction ($kg\,m^{-2}$, $kg\,m^{-1}\,s^{-1}$)
$\overset{\mathrm{Mass}}{F}$	=	time-dependent mass flux along x-direction ($kg\,m^{-2}$)
$\overset{\mathrm{Mom}}{F}$	=	time-dependent momentum flux along x-direction ($kg\,m^{-1}\,s^{-1}$)
F'_x	=	external force in x-direction (N)
$F'_{Junction}$	=	external force exerted on the junction wall in x-direction (N)
H	=	pressure head (m)
h_{loss}	=	pressure head loss (m)
i	=	cell number (–)
j	=	cell number (–)
L	=	pipe length (m)
$\dot{m}$	=	mass flow rate ($kg\,s^{-1}$)
N_x	=	the number of cells in the entire computational domain (–)
N	=	the number of cells in a pipe (–)
N_P	=	the number of pipes (–)
N_E	=	the number of elements (–)
n	=	time step index (–)
P	=	fluid pressure (Pa)
Q	=	flow rate ($m^3\,s^{-1}$)
$\boldsymbol{q}$	=	sink/source terms ($kg\,s^{-1}$, $kg\,m\,s^{-2}$)
sign(·)	=	sign function (–)
t	=	time (s)
t_{steady}	=	steady state convergence time (s)
U	=	average velocity in x-direction ($m\,s^{-1}$)
u	=	velocity in x-direction
$\boldsymbol{W}$	=	flow variable ($kg\,m^{-3}$, $kg\,m^{-3}\,m\,s^{-1}$)
x	=	position in x-direction (m)
α	=	coefficient of the external flow (m^2)
β	=	coefficient of the external flow ($m^3\,s^{-1}$)
Δt	=	numerical time step (s)
Δx	=	numerical cell (grid) size (m)
δ	=	boundary element length (m)
ϵ	=	strain (–)
ξ_E	=	error calculated from the integrated energy method (–)
ξ_{L^2}	=	error calculated from the L^2-norm method (m)
ρ	=	density ($kg\,m^{-3}$)
τ	=	collision time (s)
$\mathcal{V}$	=	volume
BGK	=	Bhatnagar–Gross–Krook
CSPM	=	Corrective smoothed particle method
FD	=	finite difference
FE	=	finite element
FV	=	finite volume
KFVS	=	kinetic flux vector splitting
MOC	=	method of characteristics
WP	=	wave plan

Funding

The research is financially supported by the Research Grant Council (RGC), Hong Kong [grants 612511, 612713 and T21-602/15R].

References

Abbott, M. B. (1979). *Computational hydraulics-Elements of the theory of free surface flows*. London: Pitman.

Aisopou, A., Stoianov, I., & Graham, N. (2010, September). Modelling chlorine transport under unsteady-state hydraulic conditions. In *Proceeding of the 12th water distribution system analysis* (pp. 613–625). Tucson, Arizona.

Axworthy, D. H. (1997). *Water distribution network modelling: From steady state to waterhammer* (Doctoral dissertation). University of Toronto, Canada.

Benson, R., Woollatt, D., & Woods, W. (1963, June). Paper 10: Unsteady flow in simple branch systems. In *Proceedings of the institution of mechanical engineers, conference proceedings* (Vol. 178, No. 9, pp. 24–49). London: Sage.

Brunone, B. (1999). Transient test-based technique for leak detection in outfall pipes. *Journal of Water Resources Planning and Management*, *125*(5), 302–306.

Chae, K. S., Lee, K. T., Hwang, C. J., & Lee, D. J. (2006). Formulation and validation of boundary conditions at a branched

junction for nonlinear waves. *Journal of Sound and Vibration*, *295*(1–2), 13–27.

Chaudhry, M. H. (1968). *Boundary condition for analysis of waterhammer in pipe systems* (Doctoral dissertation). University of British Columbia, Canada.

Chaudhry, M. H. (1979). *Applied hydraulic transients*. New York: Springer.

Chaudhry, M. H., & Hussaini, M. Y. (1985). Second-order accurate explicit finite-difference schemes for waterhammer analysis. *Journal of Fluids Engineering*, *107*(4), 523–529.

Corberan, J. M. (1992). A new constant pressure model for n-branch junctions. *Proceedings of the Institution of Mechanical Engineers, Part D: Journal of Automobile Engineering*, *206*(24), 117–123.

Duan, H. F., Lee, P. J., Ghidaoui, M. S., & Tung, Y. K. (2012). Extended blockage detection in pipelines by using the system frequency response analysis. *Journal of Water Resources Planning and Management*, *138*(1), 55–62.

Ebacher, G., Besner, M. C., Prévost, M., & Allard, D. (2010, September). Negative pressure events in water distribution systems: Public health risk assessment based on transient analysis outputs. In *Proceedings of the 12th international conference of water distribution systems analysis* (pp. 471–483). Tucson, Arizona.

Ghidaoui, M. S., & Karney, B. W. (1994). Equivalent differential equations in fixed-grid characteristics method. *Journal of Hydraulic Engineering*, *120*(10), 1159–1175.

Ghidaoui, M. S., Karney, B. W., & McInnis, D. A. (1998). Energy estimates for discretization errors in water hammer problems. *Journal of Hydraulic Engineering*, *124*(4), 384–393.

Ghidaoui, M. S., Zhao, M., McInnis, D. A., & Axworthy, D. H. (2005). A review of water hammer theory and practice. *Applied Mechanics Reviews*, *58*(1), 49–76.

Guinot, V. (1998). Boundary condition treatment in 2 × 2 systems of propagation equations. *International Journal for Numerical Methods in Engineering*, *42*(4), 647–666.

Hasler, J. (2010, February). Investigating Russian's biggest dam explosion: What went wrong. *Popular Mechanics*. Retrieved from https://www.popularmechanics.com/technology/infrastructure/a5346/4344681/

Hirsch, C. S. (2007). *Numerical computation of internal and external flows: Fundamentals of computational fluid dynamics* (2nd ed.). Amsterdam: Elsevier, ButterworthHeinemann.

Hong, S. W., & Kim, C. (2011). A new finite volume method on junction coupling and boundary treatment for flow network system analyses. *International Journal for Numerical Methods in Fluids*, *65*(6), 707–742.

Karney, B. W. (1984). *Analysis of fluid transients in large distribution networks* (Doctoral dissertation). University of British Columbia, Canada.

Karney, B. W. (1990). Energy relations in transient closed-conduit flow. *Journal of Hydraulic Engineering*, *116*(10), 1180–1196.

Kim, S. S., Kim, C., Rho, O. H., & Hong, S. K. (2003). Cures for the shock instability: Development of a shock-stable roe scheme. *Journal of Computational Physics*, *185*(2), 342–374.

Kriel, A. J. (2012). *Pressure formulation and adaptive control of numerical algorithms for transient flow in pipe networks* (Doctoral dissertation). North-West University, South Africa.

LeChevallier, M. W., Gullick, R. W., Karim, M. R., Friedman, M., & Funk, J. E. (2003). The potential for health risks from intrusion of contaminants into the distribution system from pressure transients. *Journal of Water and Health*, *1*(1), 3–14.

Liou, C. P. (1998). Pipeline leak detection by impulse response extraction. *Journal of Fluids Engineering*, *120*(4), 833–838.

Louati, M. (2013, September). On wave-defect interaction in pressurized conduits. In *Proceedings of 2013 IAHR world congress*, Chengdu, China.

Luo, J., & Xu, K. (2013). A high-order multidimensional gas-kinetic scheme for hydrodynamic equations. *Science China Technological Sciences*, *56*(10), 2370–2384.

Luo, J., Xuan, L., & Xu, K. (2013). Comparison of fifth-order weno scheme and finite volume Weno-gas-kinetic scheme for inviscid and viscous flow simulation. *Communications in Computational Physics*, *14*(3), 599–620.

McInnis, D. (1993). *Comprehensive hydraulic analysis of complex pipe systems* (Doctoral dissertation). University of Toronto, Canada.

Mesgari Sohani, S., & Ghidaoui, M. S. (2018). Mesoscopic-based finite volume solutions for waterhammer flows. *Journal of Hydraulic Engineering*. doi:10.1080/00221686.2018.1522377

Mohapatra, P. K., Chaudhry, M. H., Kassem, A. A., & Moloo, J. (2006). Detection of partial blockage in single pipelines. *Journal of Hydraulic Engineering*, *132*(2), 200–206.

Nixon, W. (2005). *Unsteady friction under the influence of external flows, and the implications to transient-based leak detection methods* (Doctoral dissertation). Hong Kong University of Science and Technology, Hong Kong, China.

Siemons, J. (1967). The phenomenon of cavitation in a horizontal pipe-line due to a sudden pump-failure. *Journal of Hydraulic Research*, *5*(2), 135–152.

Stephens, M., Lambert, M., Simpson, A., Vítkovskỳ, J., & Nixon, J. (2004). Field tests for leakage, air pocket, and discrete blockage detection using inverse transient analysis in water distribution pipes. In *World Water and Environmental Resources Congress, ASCE*, June 27–July 1, Salt Lake City, UT, USA.

Streeter, V. L., & Lai, C. (1962). Water-hammer analysis including fluid friction. *Journal of the Hydraulics Division*, *88*(3), 79–112.

Streeter, V. L., & Wylie, E. B. (1967). *Hydraulic transients*. New York: McGraw-Hill.

Streeter, V. L., Wylie, E. B., & Bedford, W. (1998). *Fluid mechanics*. Boston, MA: WCB/McGraw-Hill.

Thornton, J., Sturm, R., & Kunkel, G. (2008). *Water loss control* (Vol. *2*). New York: McGraw-Hill Professional.

Wang, X.-J., Lambert, M. F., Simpson, A. R., Liggett, J. A., & Vítkovskỳ, J. P. (2002). Leak detection in pipelines using the damping of fluid transients. *Journal of Hydraulic Engineering*, *128*(7), 697–711.

Wylie, E. B., Streeter, V. L., & Suo, L. (1993). *Fluid transients in systems* (Vol. *1*). Englewood Cliffs, NJ: Prentice Hall.

Xu, K. (1998). Gas-kinetic schemes for unsteady compressible flow simulations. *Lecture Series- Van Kareman Institute for Fluid Dynamics (VKI)*, *3*, C1–C202.

Zhao, M., & Ghidaoui, M. S. (2004). Godunov-type solutions for water hammer flows. *Journal of Hydraulic Engineering*, *130*(4), 341–348.